Alma Mater Studiorum · University of Bologna

School of Science
Department of Physics and Astronomy
Master Degree in Physics

Construction and test of a cosmic ray telescope based on CMS Drift Tube chambers and data acquisition prototypes of the Phase-2 upgrade

Supervisor:
Prof. Luigi Guiducci

Co-supervisor:
Dr. Carlo Battilana

Submitted by:
Giulia Paggi

Academic Year 2021/2022

Abstract

In this thesis work, a cosmic-ray telescope was set up in the INFN laboratories in Bologna using smaller size replicas of CMS Drift Tubes chambers, called MiniDTs, to test and develop new electronics for the CMS Phase-2 upgrade.

The MiniDTs were assembled in INFN National Laboratory in Legnaro, Italy. Scintillator tiles complete the telescope, providing a signal independent of the MiniDTs for offline analysis.

The telescope readout is a test system for the CMS Phase-2 upgrade data acquisition design. The readout is based on the early prototype of a radiation-hard FPGA-based board developed for the High Luminosity LHC CMS upgrade, called On Board electronics for Drift Tubes.

Once the set-up was operational, we developed an online monitor to display in real-time the most important observables to check the quality of the data acquisition.

We performed an offline analysis of the collected data using a custom version of CMS software tools, which allowed us to estimate the time pedestal and drift velocity in each chamber, evaluate the efficiency of the different DT cells, and measure the space and time resolution of the telescope system.

Contents

Introduction

In this thesis work, a cosmic-ray telescope was set up in the INFN laboratories in Bologna using smaller size replicas of CMS Drift Tubes (DT) chambers, called MiniDTs, to test and develop new electronics for the CMS Phase-2 upgrade. The CMS DT System is dedicated to muon identification and trajectory measurements in the barrel region. In particular, the DT system is optimized to precisely track high energy muons and to provide a robust standalone trigger with accurate bunch-crossing identification.

During the scheduled Long Shutdown 3, starting in 2026 and programmed to last 3 years, the Large Hadron Collider (LHC) will undergo the High Luminosity Upgrade (HL-LHC). In the same period, the CMS detector will also be upgraded to meet the requirements dictated by the challenging conditions imposed at HL-LHC.

The CMS detector will need to sustain unprecedented rates and particle densities and withstand such an intense radiation environment. The new system will need high resolution for trajectories and energy depositions to distinguish the products of a hard proton-proton (pp) collision from the background of soft pp interactions that will pile up in each beam crossing. The upgraded Level-1 trigger will also reconstruct the tracks from new silicon tracker detector, that can be combined with the information from the muon system and the calorimeters. However, the L1 trigger will need to maintain its standalone performance to trigger the CMS readout on tracks with large impact parameters, for which the tracker will be inefficient. This will allow to retain high selection efficiency for signatures from Beyond the Standard Model particles, which could interact weakly with ordinary matter and may decay into muons up to few meters away from the interaction point.

The present DT detector will still meet the required performance and will not be replaced for HL-LHC, but the present on-detector and the receiving back-end electronics do not meet the new trigger rate and latency specifications. Therefore, they will be replaced, and significant changes in the architectures of the trigger and readout systems will be implemented.

Using spare material from the original CMS DT chambers construction, eight small size chambers were built at INFN Legnaro laboratories. These were called MiniDTs since they have the same rectangular shape cell design as the original chambers but size of approximately $80 \times 80\,\mathrm{cm}^2$. Two MiniDTs were assembled and commissioned as part

of this thesis work and were then used to build a cosmic rays telescope in Bologna. The final purpose is to have a setup as similar as possible to the original one installed in CMS, only reduced in size. The MiniDT cells have three kinds of electrodes shaping the drift field: the anodic wire, the cathodes and field shaping strips. These are operated with high voltages set to $V_{wire} = +3600\,\mathrm{V}$, $V_{cathode} = -1200\,\mathrm{V}$, and $V_{strip} = +1800\,\mathrm{V}$ to obtain an electric field shape that guarantees the linearity of the space-time relationship, thus the resolution of the single tube. The gas mixture used is the standard CMS one made of 85% Ar and 15% CO_2. The same high voltage distribution boards and the same Front-End electronics used in CMS DTs are installed within the MiniDT gas volume. A custom board providing the low voltage and slow control of the front end, designed by the INFN Bologna electronics team, was produced to simplify the MiniDT operation.

Each MiniDT includes 64 drift tubes; LVDS signals from the Front-End electronics are brought outside the chamber using gas-tight connectors and are read by an early prototype of the On-detector Board for Drift Tube (OBDT), a radiation-hard FPGA-based board designed for the Phase-2 upgrade, providing the time to digital conversion for up to 240 channels. The OBDT is controlled and read out by a Xilinx FPGA Evaluation Board, that also provides the simulated LHC clock and slow control functionalities, mimicking the Phase-2 backend functionalities. The implemented readout is triggerless: TDC hits are continuously streamed to the backend board, buffered, and read out to a computer using an ethernet connection interfaced to the FPGA internal IPbus.

The telescope is complemented by a scintillator plane, instrumented with traditional photomultipliers read-out by standard NIM electronics. The scintillators are placed in between the two MiniDTs, to provide independent signals originated by cosmic muons crossing the system. Such signals are converted to LVDS standard using a custom conversion board and fed to the OBDT, to be digitised together with the MiniDT signals, making them available for offline analysis.

Python-based software was developed to monitor the telescope during data taking. Histograms to monitor the chamber occupancy, the timing of the signals and the rates are displayed and updated while the data taking is in progress. In addition, the combined use of MiniDT and scintillator signals enables a thorough offline analysis of the chambers' performance.

Using a version of the CMS software, modified to account for the MiniDT real dimensions and the telescope acquisition system, time pedestal calibration, drift velocity measurement, hits and segment reconstruction are implemented, allowing hit efficiency and space and time resolution to be measured. This way, the intrinsic performance of the telescope is established, enabling its use for further developments.

The thesis work is divided into 3 chapters. In Chapter 1 the CMS DT detector and its future upgrades are described. In Chapter 2 the cosmic ray telescope layout is presented and each component is thoroughly discussed. Chapter 3 is dedicated to the result of the calibration and efficiency analysis.

Chapter 1

CMS Drift Tube System

Contents

The Compact Muon Solenoid (CMS) is a general-purpose experiment that studies proton-proton and heavy-ion collisions at the Large Hadron Collider (LHC) [1].

Muons are the signature of most new physics phenomena currently under study, and they are a valuable probe for precision measurement in high-energy physics. For this reason, the CMS detector has dedicated subdetectors to identify muons, trigger on them, and provide robust and redundant measurements of their momentum over a vast range of kinematic parameters.

The cylindrical shape of the experiment allows using a coordinate system centred on the nominal collision point. The x-axis points radially toward the centre of LHC, the y-axis points vertically upward and the z-axis along the beam direction. Thus, the azimuthal angle Φ is measured in the x-y plane, on which the radial coordinate is called R. The polar angle θ is measured from the z-axis.

The core of the CMS detector is the superconducting solenoid that provides a 3.8 T magnetic field inside itself and allows to achieve high resolution for charged particles' momentum measurements. The tracking system and the electromagnetic and hadronic calorimeter are inside the magnet.

The inner tracking system relies on silicon pixels and strips for optimal resolution in vertex reconstruction.

The electromagnetic calorimeter is homogeneous, and it consists of $PbWO_4$ crystals, while the hadronic sampling calorimeter is made of plastic scintillator plates inserted between copper absorber layers.

The muon system is the outermost one, and it is integrated into the magnetic field return yoke. Given the large area to cover and the relatively low intensity of the magnetic field, it consists of gas detectors.

The system employs optimized technologies in different regions.

Cathode Strip Chambers (CSCs) instruments the endcaps due to their lower sensibility to the magnetic field, which is more intense in the forward region.

Drift Tube (DTs) Chambers cover the barrel region. These are further described in the following section.

Resistive Plate Chambers (RPCs) complement the DTs and CSCs to ensure a redundant signal, and their excellent time response is optimal for precise measurement.

For the current Run-3, gas electron multipliers (GEM) were also added to provide complementary information in the forward region. This kind of detector was chosen because it can withstand the large radiation doses that characterize CMS endcaps and can work at a high event rate.

1.1 Drift Tube system

Drift chambers could be employed in the barrel region due to a low expected rate and low residual magnetic field, below 0.2 T in most of the chambers [2].

This detection technique relies on the fact that, when crossing the instrumented volume, a charged particle ionizes the gas and electrons drift towards the anodic wire generating a signal. In the region close to the wire, the electric field is intense enough to produce secondary ionization, and thus an avalanche discharge.

Knowing the electron drift velocity in the gas mixture, the distance from the wire at which the muon crossed the tube can be calculated from the measurement of the drift time. Such distance in turn corresponds to two possible positions, either left or right of the anode wire. This ambiguity is solved at the following reconstruction stage, exploiting the presence of hits on multiple layers of drift tubes.

The distance from the wire can be computed using:

$$x = \int_{t_c}^{t_s} v_d \cdot dt \tag{1.1}$$

in which t_c is the particle crossing time, t_s is the time at which the signal is collected on the wire, v_d is the drift velocity of electrons in the cell. For most reconstruction models

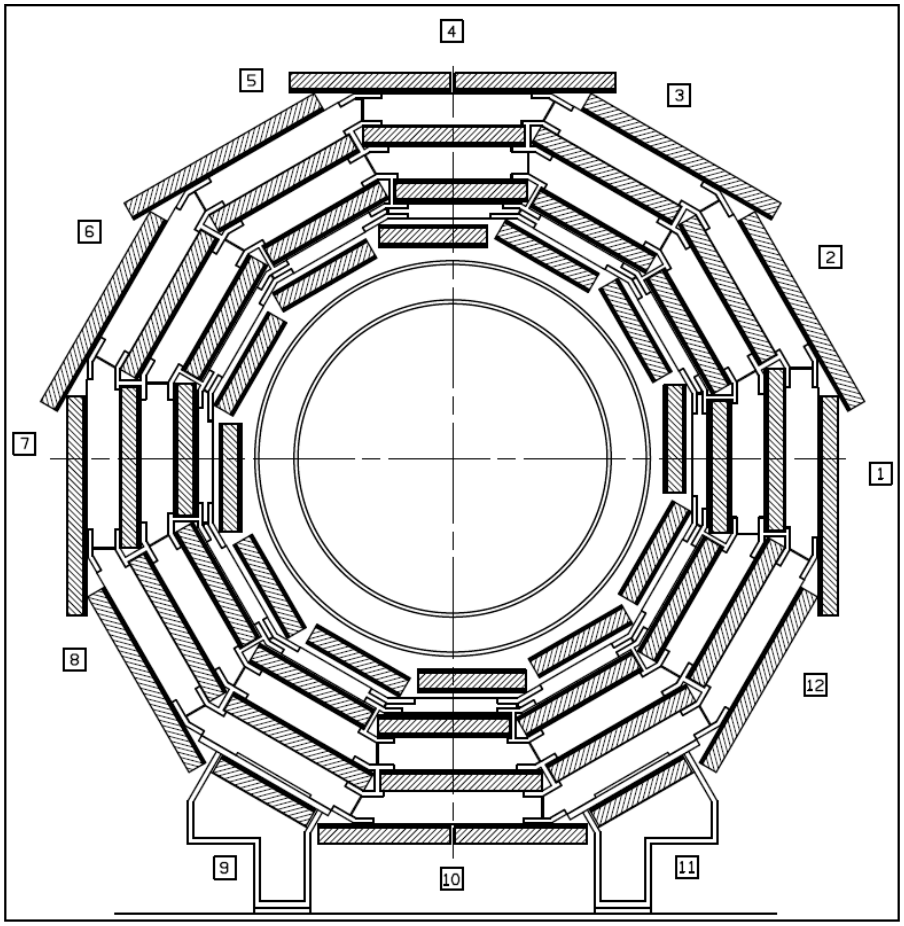

Figure 1.1: Layout of CMS barrel wheels depicting the muon DT chambers. [3]

v_d is assumed constant (see section 1.1.2) and *eq. 1.1* becomes:

$$x = (t_s - t_c) \cdot v_d \tag{1.2}$$

CMS barrel muon detector, in each of the five wheels that make up the detector, is made of four concentric cylinder stations around the beamline called MB1, MB2, MB3, and MB4 from inside out, shown in *Fig. 1.1*. The first three consists of 60 drift chambers each, while the outer one has 70. Each wheel is further segmented into 12 sectors covering about 30° in the azimuthal view.

1.1.1 Chamber Design

A CMS DT chamber is made of three independent units, called SuperLayers (SL), except for MB4 chambers which consist of two SuperLayers. A SL is a group of four consecutive

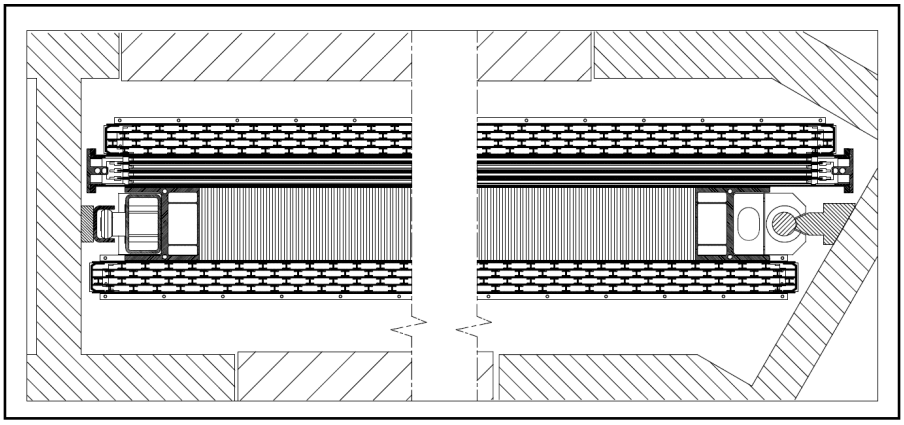

Figure 1.2: Drift Tube Chamber inside the iron yoke, cut in the (R, Φ) plane. The Φ SLs are on the top and bottom of the chamber. The θ SL can be identified by the different wire direction. In between the SLs, the honeycomb structure provides mechanical support.

layers of tubes, staggered by half a cell so that the correlation between the drift time in different planes allows the computation of coordinates and angle of the crossing tracks. Three independent layers would be sufficient for segment identification inside an SL, but a fourth layer ensures redundancy and robustness to reconstruction methods and the local trigger system [4].

Each SL is made of four layers of rectangular drift cells staggered by half their width, with the mechanical support of five 2 mm thick aluminum sheets separated by the insulated aluminum I-beams that separate the cells from one another.

In a chamber, two SLs, called Φ SLs, are oriented with the wires parallel to the beamline and measure the coordinates in the (R, Φ) plane. The third one, the θ SL, is rotated by 90° and measures the z coordinate. This choice was made to have a redundant detection system in the (R, Φ) plane to accurately reconstruct the trajectory of a curved track. In the η view, a single SuperLayer is capable of reaching the desired accuracy. Moreover, due to economical reasons, the θ SuperLayer is missing in MB4 chambers that only consist of the two Φ SLs.

To achieve a better direction resolution, the two Φ SL are not contiguous but are spaced by about 23 cm. In between them, there are the θ SL and a 128 mm thick aluminum honeycomb plate that also provides mechanical stability to the chambers. The transverse view of a DT chamber inside the iron yoke can be seen in *Fig. 1.2*.

1.1.2 Cell Design

The base element of the DT chamber is the drift tube. It has a 42 mm pitch and is 13 mm thick, as shown in *Fig. 1.3* [3], while the wire length is $\sim$ 2.5 m, due to the constraints imposed by the barrel longitudinal segmentation.

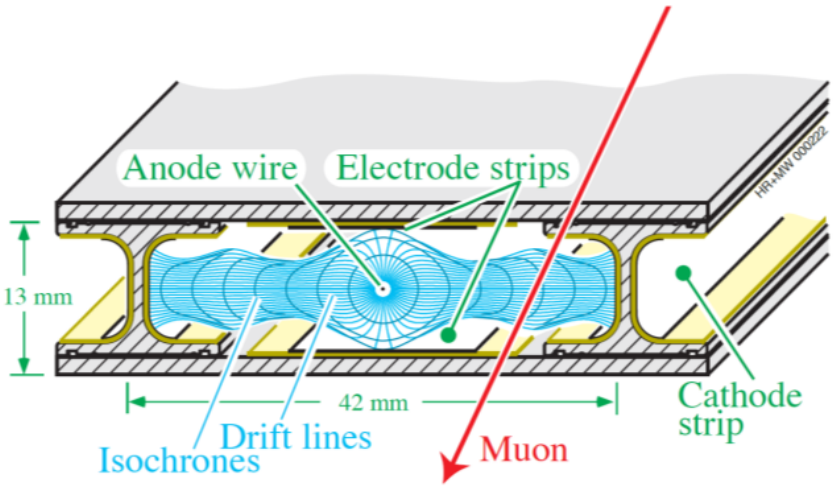

Figure 1.3: Schematic view of a single drift tube. The shape of the nominal electric field lines is also shown.

The dimension of the drift cell is such that the detector occupancy is very low. At the same time, it is large enough to limit the number of total channels, so that the barrel muon system consists of about 172000 active wires. In each cell, there are five electrodes: the anodic wire that collects the signal, two strips that shape the drift field, and the cathodes which are on the I-beams that separate the cell from one another. This design allows for a good performance even if stray magnetic fields are present in some regions of the chambers.

The anode wire is a 50 μm diameter stainless steel wire, gold-plated to avoid oxidation. The cathodes are aluminum strips, insulated via a mylar layer, located on both sides of the grounded I-beams, which are 1.2 mm thick and 9.6 mm high.

A pair of strips further shape the drift field to improve the linearity of the time and space relationship and thus the resolution of each cell. *Fig. 1.3* also shows the expected electric field inside one cells obtained with high voltages set as $V_{wire} = +3600\,\mathrm{V}$, $V_{cathode} = -1200\,\mathrm{V}$, and $V_{strip} = +1800\,\mathrm{V}$.

The gas mixture is made of 85% Ar and 15% CO_2. Argon is a noble gas, hence it has no electronegativity. This property is relevant in a gas detector since one wants the electron to drift inside the chamber without being captured. On the other hand, carbon dioxide acts as a quencher absorbing most of the photon produced in the avalanche and its presence allow for a larger efficiency plateau before discharges occur in the gas.

The chosen ration in between Ar and CO_2 allows for good quenching while saturating the drift velocity of electrons to preserve the space-time relationship linearity. When choosing the gas mixture, safety requirements, cost, and impact of chamber ageing were also considered. These gases satisfy all the conditions. In particular, they are nonflammable, their cost is low, and no organics component can contribute to the

deposition of material on the anodic wire.

Given the voltages of the electrodes in a cell, the saturated drift velocity is about $54\,\mu$m/ns, resulting in a maximum drift time of about 380 ns. A single DT cell has a detection efficiency of $\sim 98\%$ and an intrinsic spatial resolution of $\sim 200\,\mu$m.

The high voltage (HV) and the front-end (FE) electronics are located at opposite ends of the wires. For this reason, the gas enclosures are different. On the high voltage side, in addition to the gas outlet, it contains the HV and the test pulse distribution system. While on the front-end part, it contains the gas inlet together with the HV decoupling capacitors and the FE circuitry with the associated cooling system.

This results in different dead areas on the two sides of one chamber, where one considers a dead area the distance between where the wire enters the end plug and the outer face of the gas enclosure.

The choice of including electronics inside the gas enclosure stems from the need to reduce connection complexity, dead space, noise, and crosstalk. The front-end electronics are separated from the HV distribution circuitry both for insulation problems, and to better employ the space inside the aluminum enclosure and reduce dead space. Moreover, with this design, the chamber provides a unique ground reference for high voltage and signals.

The gas distribution in a SuperLayer is through each cell, with the input at the front end and output on the HV side. In particular, two inlets are at the sides of the chamber that are connected to a distribution bar with many small holes to equalize the impedance inside the chamber and minimize the pressure drop. Gas tightness of the SLs is crucial because contamination by the nitrogen or molecular oxygen present in the air can strongly alter the electron drift velocity. To ensure the gas tightness, when assembling the SLs the aluminum profiles are glued to the outer aluminum casing, while O-rings seal the front and back plates containing the gas and HV connectors, and signals output. Before closing the structure, reference blocks are also glued along the sides of the SL in a way that the wire positions with respect to them are precisely known.

In addition, in each SL's gas enclosure one can find pressure and temperature sensors to monitor the chambers, and ground straps that short-circuit all the aluminum planes to have a unique ground reference for the signals in addition to the front-end electronics and the HV distribution system. Thus, each SL is an independent chamber.

1.1.3 SuperLayer Construction

To assemble a SL, a complete layer of cells is built at the same time.

The aluminum I-beams, wires, and plates were prepared beforehand with dedicated tools.

In particular, the insulation is crucial to employ the I-beams as cathodes. The first design described in [3] foresaw extruded Lexan profiles glued on the top and bottom of the

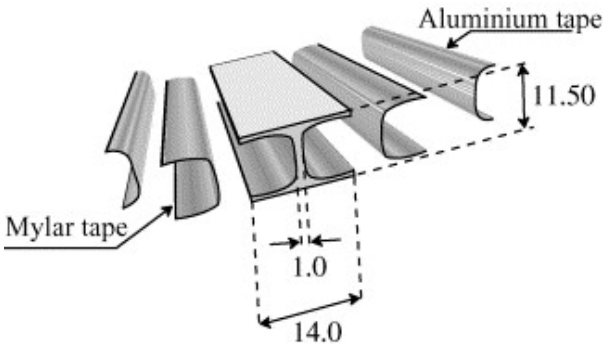

Figure 1.4: Exploded view an I-beam with insulators and cathode strips.

I-beams. This configuration did provide good electrical results but suffered mechanical weaknesses.

The new design, shown in *Fig. 1.4* uses I-beams with wider wings to increase the glue joint surface, and in this configuration, the I-beams are glued to the aluminum plates [5]. This procedure allows reducing the number of glueing and increases the mechanical strength of the final configuration. The I-beams are then at ground voltage as the SL aluminum cage.

The cathodes are placed on both sides of the I-beams. In particular, a cathode is a 50 μm thick, 11.50 mm wide aluminum tape, electrically insulated from the I-beam by a 100 μm thick, 19 mm wide mylar tape to have a guard-ring of at least 3.5 mm between the electrode and the I-beam. Both the conducting and insulating tapes are self-adhesive with pressure-activated glue. The cathodes are connected to the high voltage via metallic springs.

The new cathode configuration requires spark protection at the ends of the cathode strips. The plastic end plugs that hold the block in which the wire is crimped were redesigned to offer this discharge protection. These components extend from within the cell, adding 12 mm of protection around the wire.

Before constructing one layer, all needed wires are tensioned at 3.2 N and crimped on solid copper-tellurium blocks of 4 mm side. The blocks have a 0.1 mm wide, 0.3 mm deep groove in which the wire is placed. The crimping procedure consists in applying pressure on 70% of the groove length to deform a small region of the block so that it encases the wire without damaging it. The blocks are inserted into plastic end-plugs to be glued to the aluminum plates to define the wire position with respect to each other and in the chamber.

The aluminum plates are prepared by glueing the strip electrodes onto them. These electrodes are obtained using a 14 mm wide and 70 μm thick aluminum strip glued onto mylar tape strips 0.1 mm thick and 20 mm wide. As in the cathode design, the mylar strips are wider to prevent sparking between the copper and the aluminum plates.

A computer-controlled machine puts the strips in the correct position on the aluminum layer since they need to be within 0.5 mm from the design position.

The SuperLayer assembly is done on a precision table with reference points for the different tools needed for the procedure.

In a single step, a whole layer of I-beams, equipped to be cathodes, are glued to the aluminum sheets with applied field-shaping strips. This procedure is done with a dedicated tool that fixes the cathode position at the nominal value. The same tool also puts in place the plastic end-plugs that define the wire pitch, since their position must be known with a precision of 0.1 mm. The glue used is Araldite and is applied using the same computer-controlled machine that lays strips onto the aluminum planes.

Once the I-beams are positioned, pressure is applied until the glue polymerizes. The procedure must be repeated on both sides of the plate.

Wires can then be placed on the layer. The crimping block, with the wire already in position, is placed into a plastic wire holder, and then inserted between two glued end-plugs. The wiring is done manually. Before closing the layer by glueing the top aluminum plate, it's necessary to

- insert the HV contact for the I-beam through the end-plugs;
- check the wires tension;
- check the strips HV contacts;
- measure the wire positions;
- point-weld the ground straps.

The procedure is repeated to complete the four layers.

Before glueing the fifth layer and completing the SL, one needs to glue some aluminum pieces that will be the corner blocks of the gas-tight box, at a known position with respect to the wire.

Once the SL structure is assembled, the construction ends by installing the HV boards and test pulse distribution system, the HV decoupling capacitors, and the amplifiers and discriminators for the FE side. After this, the front cover plate is closed and the SL is completed.

1.1.4 SuperLayer Electronics

High Voltage The HV is distributed using six-layers printed circuit boards (PCB). Each layer provides the HV to one type of electrode of 8 cells in the same plane. Thus in total, one PCB provides the HV to 16 cells, 8 per layer in 2 adjacent layers. The voltages are distributed using 50 MΩ resistors: one per wire and one for every pair of two strips or cathodes. A distributed ground surrounds all connections in the different layers,

which are also staggered to avoid crosstalk among the various electrode connections. The connections are made with short wires.

The PCB is secured to the aluminum plate between layers by three spring connections that serve as both mechanical support and a ground connection. HV inputs of the PCBs can be daisy-chained so the number of cells powered by a single primary line will depend on the segmentation in the HV distribution tree.

The PCBs also have a Test-Pulse system: two strip-lines are embedded and AC coupled via a 1pF capacitance to the wire connections of one cell plane. The two strips can be independently operated and can inject voltages of variable amplitude. The test pulse system is used to calibrate the DT chambers with simulated signals emulating vertical tracks.

Front End The first step of the FE circuitry consists of PCBs, one for 4 channels on the 4 layers, that have HV decoupling capacitors, connected to the anodes via a short wire. As for the HV side, the PCBs are fixed to the central aluminum plate with spring contacts that provide mechanical support as well as a ground connection. The decoupling boards are connected to the FE boards (FEB) via strips of contacts. The FEBs are multilayer PCBs to have the input and output lines on different layers, separated by a ground plane. FEBs also have a temperature sensor and a trimming circuit for the thresholds. A common threshold line connects all of the FE PCBs in an SL.

The front-end electronics amplify the signals from the detector, compare them to a threshold and send the output logic signal to the following part of the readout chain. The amplifier must have low noise to allow operating the DT at low gain, which is essential for the chambers' lifetime. Moreover, it must have a fast shaping time not to worsen the spatial resolution. The comparator has to be fast and precise so that the time response is independent of the signal amplitude.

Readout and Trigger The readout and trigger electronics [6] share the output signal of the chambers, and Timing and Trigger Control (TTC), which distributes the system clock. They also have the same power supply, cooling, and mechanics.

The signals provided by the chambers' FE are received by the Read Out Boards (ROB). A ROB consists of four 32-channels TDC and can thus process up to 128 signals. Before they can be used as ROBs input the LVDS signal from the FE must be converted, using 32 4-channel differential line receivers. The ROBs rely on the ASIC HPTDC (High Performance Time to Digital Converter) to perform the time to digital conversion of the hits coming from the chambers and assign them to the Level 1 trigger.

The ROBs are hosted inside a Minicrates (MiC). A MiC is an aluminum profile with support structures to provide cooling to the electronics hosted inside. In the Minicrate, the ROBs are integrated together with the muon trigger electronics and the Chamber

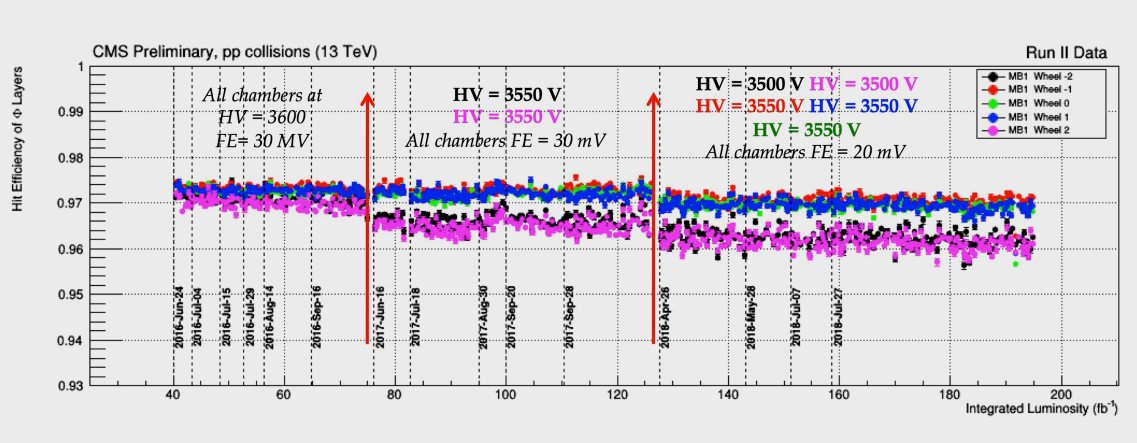

Figure 1.5: Φ layers efficiency as a function of the integrated luminosity of the innermost DT chambers. The HV and FE threshold settings for each data taking period are also shown.

Control Board (CCB).

The ROBs' output used to be transmitted to the Read Out Server (ROS) boards, which merged information from the 25 ROBs of the same sector, i.e. a 30° azimuthal region of one of the detector wheels. The time needed for a ROS to build an event depended on the hits' distribution in the ROBs, thus the maximum acquisition rate decreases as the instantaneous luminosity, so background and muon hit rates, increases.

For this reason, during the 2017-18 technical stop, the ROS were replaced with the μROS [7], a new version based on the μTCA technology [8]. The μROS is implemented on the same board, programmed with a different firmware, designed for the TwinMux [9] that instead is part of the Phase-1 L1 Trigger system [10]. The TwinMux combines information from the DTs that provide excellent position resolution and barrel RPCs that have optimal timing resolution as the Phase-1 L1 Trigger's guiding principle is to use as soon as possible all detectors traversed by a muon for online reconstruction to maximize the trigger performance.

1.1.5 Performance at LHC

CMS DT chambers' performances have been thoroughly studied using both cosmic rays and collision data collected during the most recent Run-2 [11].

Fig. 1.5 shows the efficiency of the Φ layers of the innermost chambers, the MB1s, as a function of the integrated luminosity. The variations visible in the chart depending on two factors:

- the ageing of the chambers, the MB1s, especially in the outer wheels are exposed to the most radiation;

- changes in the detector configuration, in particular the lowering of the HV.

As can be seen in the picture, already with 2016 data in wheels ±2 a trend of efficiency loss can be identified. One can see how in 2017 the MB1s were operated with lower HV to slow the ageing process. In 2018, to balance the even lower HV setting, the FE thresholds were reduced as well, allowing to maintain the efficiency of $> 95\%$.

For each crossing particle, the SLs perform the bunch-cross tagging independently and return the position of the center of gravity and angle of the track segment to the first-level muon trigger for the assignment of time and transverse momentum.

The spatial resolution is quantified using the distribution of residuals of the reconstructed and expected hit position. As shown in *Fig. 1.6* the space resolution of each chamber computed at the beginning and the end of LHC Run 2. In Φ superlayers is better than $250\,\mu$m for MB1, MB2, and MB3, better than $300\,\mu$m in the MB4. The resolution of the Φ superlayers is worse in MB4 because no θ measurement is available, so no corrections can be applied to account for the muon time of flight and the signal propagation time along the wire. In θ SLs the resolution is in between $250\,\mu$m and $600\,\mu$m, except for MB1 [12].

The different trend from wheel 0 to the outer ones can be explained considering that in θ superlayers as the inclination angle increases, the linearity of the distance-drift time connection worsens, reducing resolution, while in Φ superlayers the inclination angle increases the track path within the tube and improves the resolution.

DT chambers can achieve a time resolution of a few nanoseconds, providing excellent time measurements. Using muons reconstructed in the barrel, the time resolution can be estimated from the distribution shown in *Fig. 1.7*.

The position of each element with regard to the others must be determined with the greatest accuracy possible to accomplish this performance, hence the procedure for assembling the SLs is critical.

The excellent position and time resolution allow the DT to noticeably improve the momentum resolution that can be obtained when reconstructing muons tracks.

An example is a *Fig. 1.8* which reports the relative residual for cosmic rays muons [12]. Red markers show the resolution obtained using only information from the pixel tracker, while the black ones are obtained including the muon system in the computation.

The DTs contribution is relevant especially at high momentum, for example at $\sim$ TeV the resolution can be reduced from $\sim 10\%$ to about $\sim 6\%$.

1.2 Future Phase-2 Upgrade

LHC has scheduled the Long Shutdown 3 to start in 2026 and to last 3 years. During this period, the CMS detector will be upgraded to meet the performance needed to properly work under the challenging conditions imposed by the LHC High Luminosity upgrade [13].

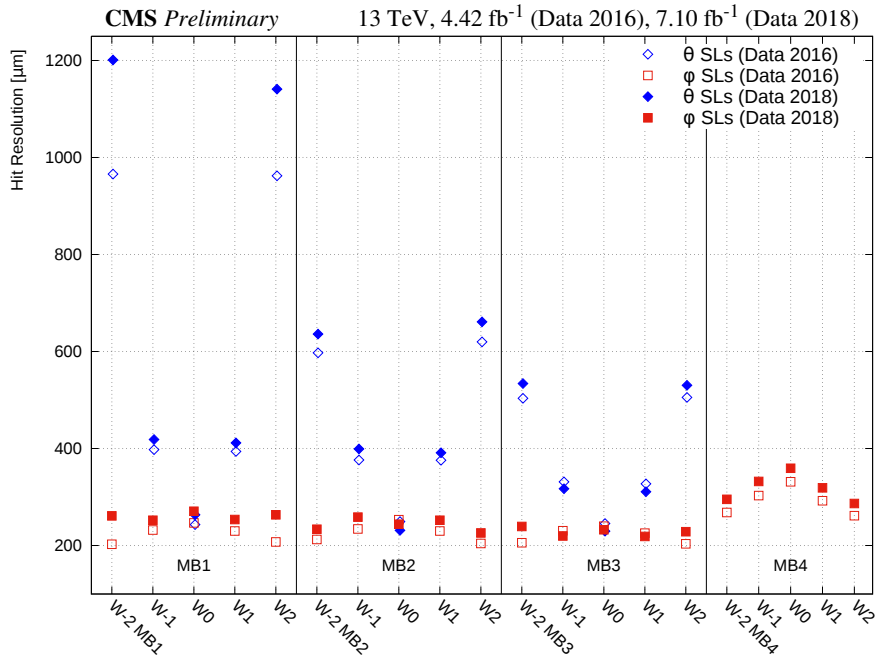

Figure 1.6: Reconstructed hit resolution for DT as a function of station and wheel. Φ superlayers are represented by squares and θ superlayers by diamonds. The plot shows the resolution at the beginning (hollow markers) and the end (full markers) of Run 2. The worsening of the resolution is due to lower HV, to slow the ageing of the chambers. The uncertainties in these values are smaller than the marker size in the figure. [12]

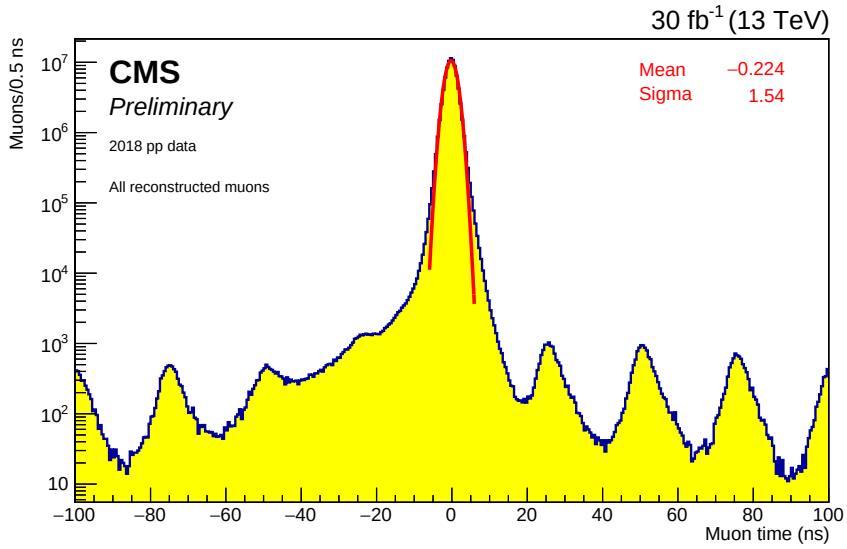

Figure 1.7: Time-at-vertex distribution for muons from collisions in the barrel, reconstructed using DT chamber.

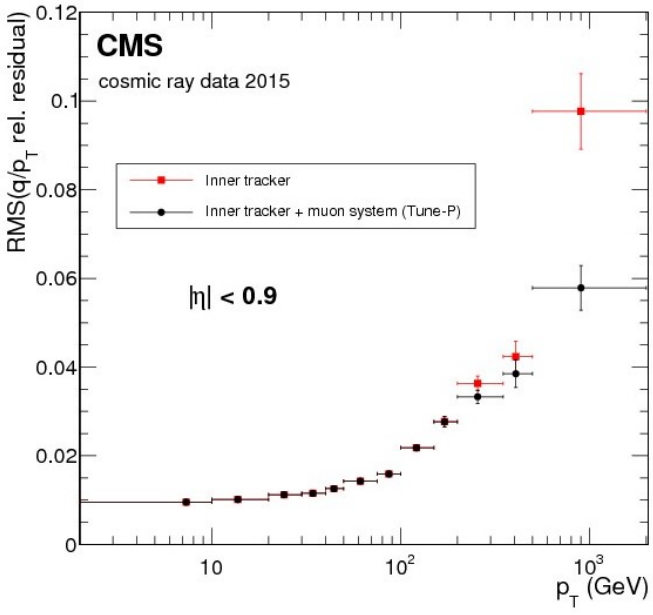

Figure 1.8: Resolution of the relative momentum as a function of the momentum. In red, the values obtained using only the inner tracker information, in black the ones in which the muons system information is also considered.

Indeed, HL-LHC will produce more than 200 proton-proton (pp) interactions for each bunch crossing, taking place every 25 ns, resulting in several billions of secondary particles per second. As a consequence, the CMS detector must be able to cope with the high rate and density, withstanding such an intense radiation environment.

In particular, the new system will need high resolution for trajectories and energy deposition to distinguish the hard proton collision from the soft background that will pile up in each beam crossing. To maintain the current performance level, the whole muon system must take into account [14]:

- the high particle flux impact on the ageing of the gaseous detector and of the electronic components that will not be replaced;

- the resolution and redundancy needed to distinguish the large number of particles crossing the CMS detector almost simultaneously. The reconstruction of a single track can be done only if the number of hits recorded is adequately large and time and spatial resolution are very good. Event reconstruction is crucial for both the online muon trigger and the offline analysis;

- the momentum measurement precision for a standalone muon trigger. This information is necessary to look for long-lived beyond Standard Model particles that decay outside the inner tracker, thus the trigger can not rely on tracker information;

- the extended coverage of the Phase-2 inner tracker needs to be matched by an extension of muon detector since the silicon tracker cannot identify muons;

- the high rate at which the electronic must be able to work. It can be achieved by relying on new technologies such as high bandwidth optical data transfer. The Level-1 trigger and data acquisition must also be upgraded to meet the latency requirement, enhancing buffers and processing speed.

Regarding the Muon Drift Tubes (DT) System, the upgrade focuses on the replacement of the on-detector electronics and its associated back-end electronics.

In the present configuration, The Muon DT System is dedicated to muon identification and momentum measurements in the barrel region. The DTs also provide a robust standalone trigger with accurate bunch crossing identification.

In the Phase-2 upgrade, the muon trigger will need to be integrated with the new tracker system while retaining its standalone performance to trigger tracks with large impact parameters, for which the tracker will be inefficient. The present DT system will not be changed for HL-LHC, thus the goal is to maintain the present performance even with the HL-LHC background rate and the trigger and data acquisition rate ($500 - 750$ kHz L1 trigger rate and $12.5\,\mu$s L1 trigger latency). The present on-detector electronic, the Minicrates (MiC), do not meet these requirements. Therefore, the MiC and the receiving back-end electronics need to be replaced.

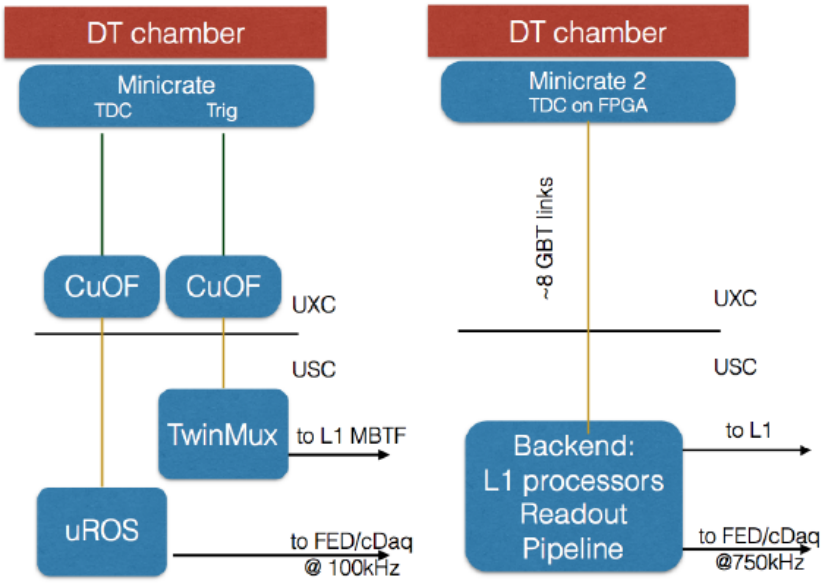

Figure 1.9: Scheme of DT readout system in the current (left) and Phase-2 Upgrade (right) configuration. The green lines represent wire connections, while the yellow ones links obtained with optical fiber.

The Phase-2 readout architecture, schematically reported in *Fig. 1.9*, will rely on the continuous streaming of the TDC measurements to the back-end electronics so that the on-detector components are minimal. Each SuperLayer will be read by one OBDT (On-Board Electronics for DT), or two in the case of the largest MB3 and MB4 SuperLayers.

These should only provide:

- LHC Clock and fast signal distribution (BGO commands), including Bunch Crossing Zero (BC0);
- data transfer to UXC via optical links;
- time digitization of the analogue signals from the Front End Boards;
- control of the FEBs;
- test pulse generation;
- monitoring of the DT chamber sensors (temperature, pressure, etc.) ;
- slow control services for the RPC and alignment systems.

Thus, the trigger primitive generation, done by the read-out and trigger boards in the present configuration, will be performed on boards located outside the experimental cavern, where the environmental conditions are less extreme and the electronics are always accessible. The simplification of the Minicrates electronics will benefit the entire DT LV system by lowering on-detector electronics power consumption and hence boosting the durability of both the FEB and the MiC. Furthermore, the new architecture will benefit from the new and improved electronics to achieve better performance.

The first prototypes of the HL-LHC electronics, the on-detector board, have been installed in the DT chambers of one sector and integrated into the central data acquisition and trigger systems. The signals from the chambers are split via specifically designed splitter boards that preserve the signal integrity, so that the legacy and Phase-2 Slice Test demonstrator can operate in parallel during LHC collisions [15].

Chapter 2

Cosmics-rays telescope

Contents

The telescope system consists of two small-size replicas of CMS DT chambers, called MiniDTs, and 9 scintillator tiles, each equipped with two photomultipliers, that can be arranged in one or more layers.

The system is located on an aluminium structure that provides support for the detector and the electronics making up the readout system. The frame is also instrumented with a flowmeter to adjust the flux of gas flowing in the chambers. Next to the flowmeter, a glass bubbler connected to the chamber's output, ensures that the pressure inside the MiniDTs is higher than the atmospheric one. This minimizes the probability of air leaking into the chambers, even in the case of small leaks due to issues in the MiniDT assembly phase.

In the following section, the MiniDTs and the scintillator planes will be further discussed, as well as the readout system and the data acquisition and online monitoring software.

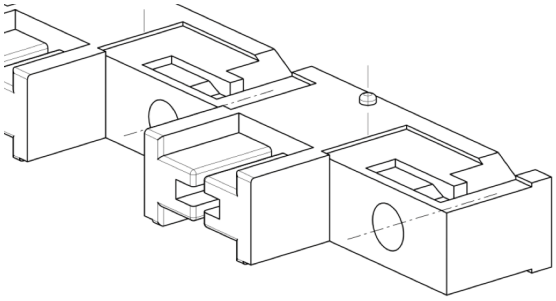

Figure 2.1: Schematic representation of the MiniDTs' endcaps.

2.1 MiniDT Chambers

Two smaller-size SLs called MiniDTs were built at INFN Legnaro Laboratory in Padova, using spare material from the original CMS DT chambers.

As in the original ones, a SuperLayer consists of 4 layers of parallel rectangular drift tubes.

In the case of the MiniDTs, each layer has 16 drift tube cells, for a total of 64 in a SuperLayer. The MiniDTs wire length is about 0.5 m. Thus, considering the electronics and the aluminium enclosure each chamber has a dimension of about $80 \times 80\,\mathrm{cm}^2$.

The cross section of drift tube cells in MiniDTs are in all identical to the ones of CMS DT chambers, and they are operated with the same gas and the same high voltages. The gas is a mixture of 85% Ar and 15% CO_2, while the voltages applied to the anodic wire, cathodes and field-shaping strips are $V_{wire} = +3600\,\mathrm{V}$, $V_{cathode} = -1200\,\mathrm{V}$, and $V_{strip} = +1800\,\mathrm{V}$. This allows for a drift field shaped as described in section *1.1.2*.

The two MiniDTs used in the telescope are MiniDT 7 and MiniDT 8, whereas the first six are used in the Legnaro National Laboratories.

2.1.1 MiniDT Construction

The MiniDTs construction is done generally following the procedure for the construction of CMS DT chambers, reported in section 1.1.3.

The main differences are related to the presence of more manual assembly operations.

The small number of chambers to be produced would not justify the cost of the construction of specialised and automatic tools, also considering that their size and weight make them easy to handle on a precision table.

To ensure alignment between layers, holes were machined into each aluminium sheet of the stack by a CAM, and reference pins are fixed to the working table.

In addition, some of the chamber elements were redesigned to facilitate the detector construction while ensuring a precise alignment of the cathodes, wires and strips with the use of external positioning tools.

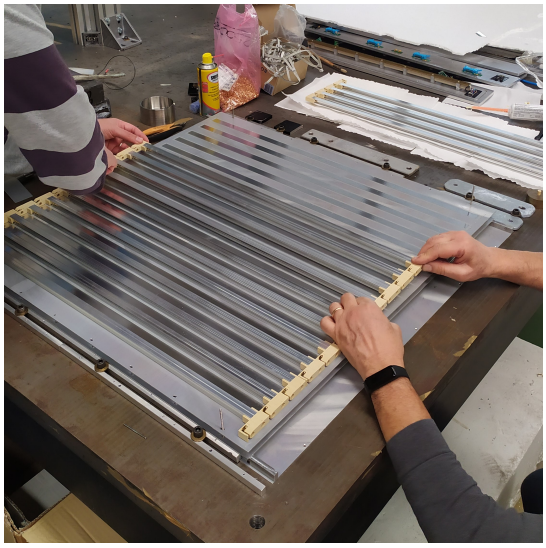

Figure 2.2: Positioning of a group of four cathodes onto the aluminium sheet.

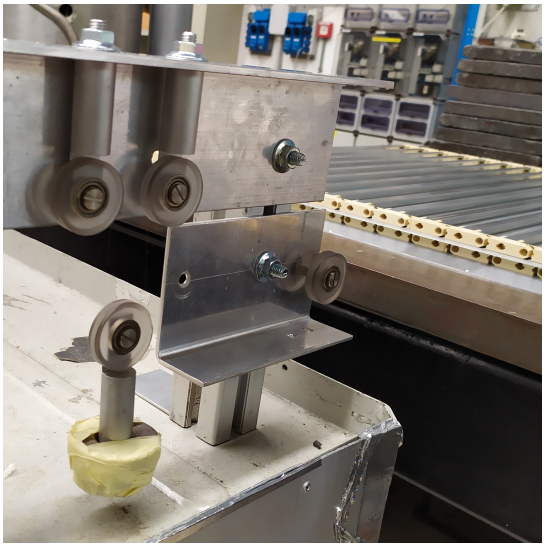

Figure 2.3: Tool used to tension the wires during the MiniDTs' assembly.

For example, the INFN physicists and technicians developed a new version of the cells' endcap, holding the crimping block, which can be seen in *Fig. 2.1*. The MiniDTs design exploits the aluminium sheets preprocessing to have precisely located holes, in which an endcap holding together a group of four cathodes fits. This allows for better alignment of the cathodes in the chamber and between each other. *Fig. 2.2* shows how the endcaps are positioned onto the aluminium layer.

In the MiniDT case, the wire plugs are truncated cones developed to fit the new endcap design. These are made of insulating material, namely Noryl resin reinforced with glass fibers, and have a small hole to insert the metallic pipe onto which the wire is crimped. This part has a wider section to maintain the correct position with respect to each wire plug. In this way, the crimping pipe also serves as the pin to connect the FE circuitry. To avoid pin misalignment when connecting and disconnecting the electronics, the pin is glued to the endcaps using Araldite 2011.

The crimping of the wire is done manually after positioning the wire and tensioning it with a dedicated tool shown in *Fig. 2.3*.

Instead, strips and cathodes were already applied as described in section 1.1.3, since the spare aluminium sheets and I-beams from the CMS DT chamber construction were used, once cut to the desired shape.

Nevertheless, the mylar and aluminium strips were manually cut to the proper shape on each side and at the ends to prevent sparking within the chamber.

After each layer's glueing, some lead blocks provide pressure and ensure uniform contact between all parts to be glued together.

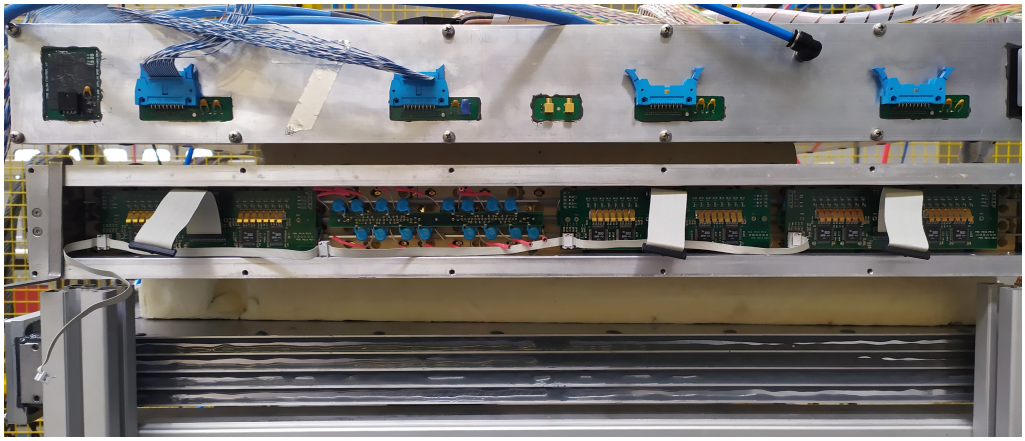

Figure 2.4: MiniDT FE circuitry. Only three out of the four FEBs were applied at the moment of the photo, showing the HV decoupling capacitor boards.

After assembling a MiniDT, it is tested to identify any potential issues:

- gas tightness test: the gas tightness is checked by flushing gas into the chamber and estimating the maximum height of a water column that allows the gas to exit the chamber, knowing that 1 cm of water is about 100 Pa;
- high voltage distribution boards installation: the HV board and the corresponding HV decoupling capacitor are connected;
- high voltage test in air: the MiniDT is powered and tested for sparks or short-circuits in air;
- high voltage test in Ar-CO_2: the test performed with air within the chamber is repeated once it is filled with the Ar-CO_2 gas mixture;
- Front End Boards installation: when the MiniDT behaviour is stable filled with the gas mixture and the high voltages on, the FEBs are added and the chamber can be used to read data and commission each channel.

Even if this process requires each MiniDT to be filled with gas twice, thus resulting in the Ar-CO_2 mixture waste, it is necessary to avoid any possible FEBs breakdown.

After these tests, the MiniDT is powered and data are taken to identify any remaining faults or malfunctions.

2.1.2 MiniDT Electronics

The electronics of the MiniDTs on both the HV and FE sides are the same used in the original CMS chambers, described in section 1.1.4.

For example, *Fig. 2.4* shows a MiniDT FE circuitry: one of the HV decoupling boards can be seen, while the other three are hidden by the FEBs.

Nevertheless, the MiniDTs have a custom HV connector, shown in *Fig. 2.5*, for connecting to various HV boards. This connector allows for the partitioning of a chamber so that if a cell experiences issues that make it unsuitable for data taking, the corresponding section of the MiniDT may be easily turned off.

In particular, in a MiniDT, each layer of strips and cathodes could be powered independently. For the wires, an even finer segmentation was implemented: each half layer could be operated separately.

For the telescope setup, an HV splitter box for each MiniDT was built, to interface standard HV power supplies with the on-chamber HV connector.

Such boxes feature three standard coaxial HV connectors, corresponding to anodes, cathodes and strips, and a multiconductor HV cable to plug into the MiniDT. Within the box, HV is distributed to all partitions mapped onto the MiniDT HV connector, as long as no problems require disconnecting any of them.

In the telescope setup, a CAEN 1527 Power Supply System is employed, and it is instrumented with an A1561H Power Supply Board providing both positive and negative outputs.

The low voltage powering and control of the Front End electronics in CMS Drift Tubes chamber is based on a system of so-called *Splitter Boards*, developed to implement the complex, distributed powering of multiple, large chambers in CMS. To simplify the operation of the MiniDTs, a custom board was designed in Legnaro and developed and implemented by the electronics service of INFN Bologna. This board, called Low Voltage Front End (LVFE) and shown in *Fig. 2.6*, is powered with a 12 V bench power supply and provides all needed voltage levels to the FEBs. It handles the configuration and monitoring controlling the chamber I2C bus and can generate the voltage levels for the FE discriminator using DACs. The LVFE board is controlled by a simple USB to I2C adapter, using a Labview program.

For the present work, the threshold value was set at 100 mV.

2.2 Scintillators

Scintillators are used to complete the telescope set-up and provide an independent signal of particle crossing the instrumented volume.

The Bologna INFN technicians assembled 12 scintillators, shown in *Fig. 2.7*, encased in aluminium sheets, each instrumented with two photomultipliers (PMTs). The scintillating material and the photomultipliers were upcycled from the DELPHI experiment.

The scintillating material is a 579 mm long, 10 mm thick plane, curved on one side so that the width is in the range between 80 mm and 110.04 mm, as shown in the technical drawing in *Fig. 2.8* and in the 3D model in *Fig. 2.9*. On the straight side, 15 wavelength

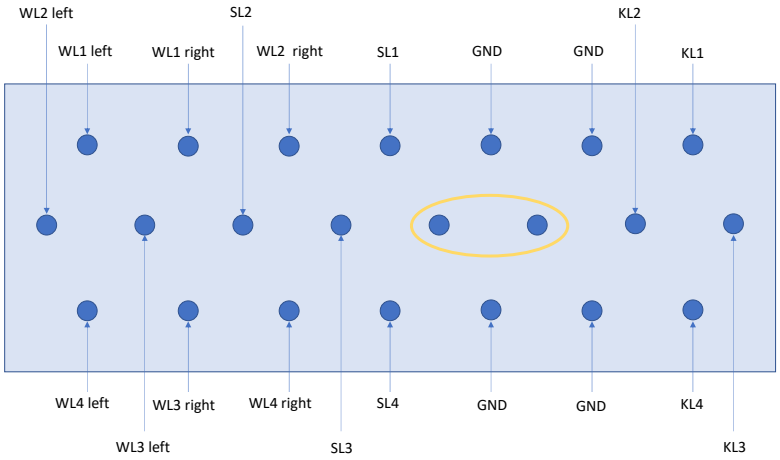

Figure 2.5: Scheme of the internal view of the HV connector. Each pin is connected to either the wires (W), the strips (S) or the cathodes (K) of one of the four layers (L1-L4). The wires input is segmented in order to divide the left and right halfs of the chamber. The pins circled in yellow are not connected and can be used as an interlock.

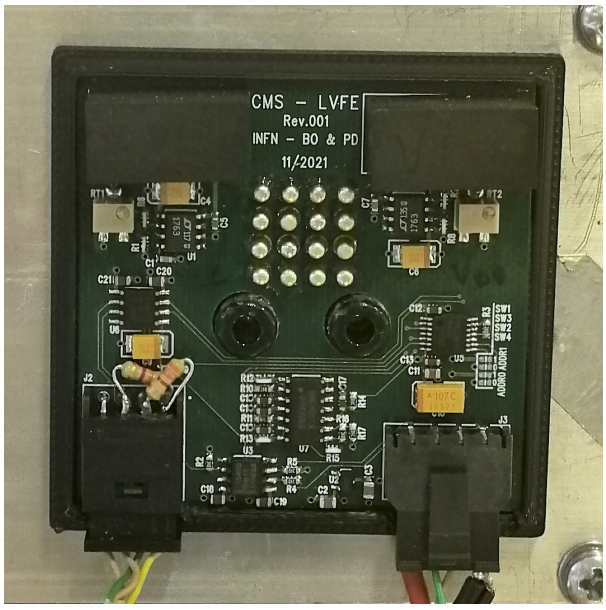

Figure 2.6: LVFE board in use on one of the MiniDT chambers in the telescope setup.

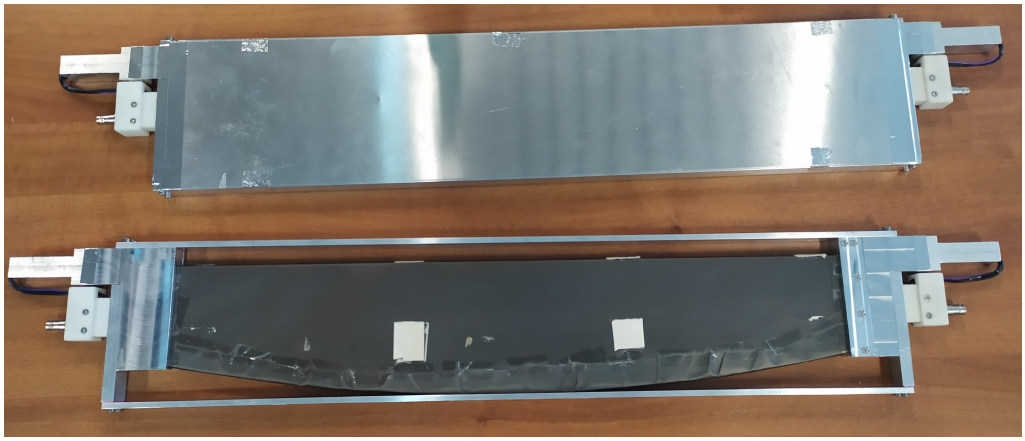

Figure 2.7: Scintillators used in the telescope set up. The bottom one shows the shape of the scintillating material enclosed in the aluminium case.

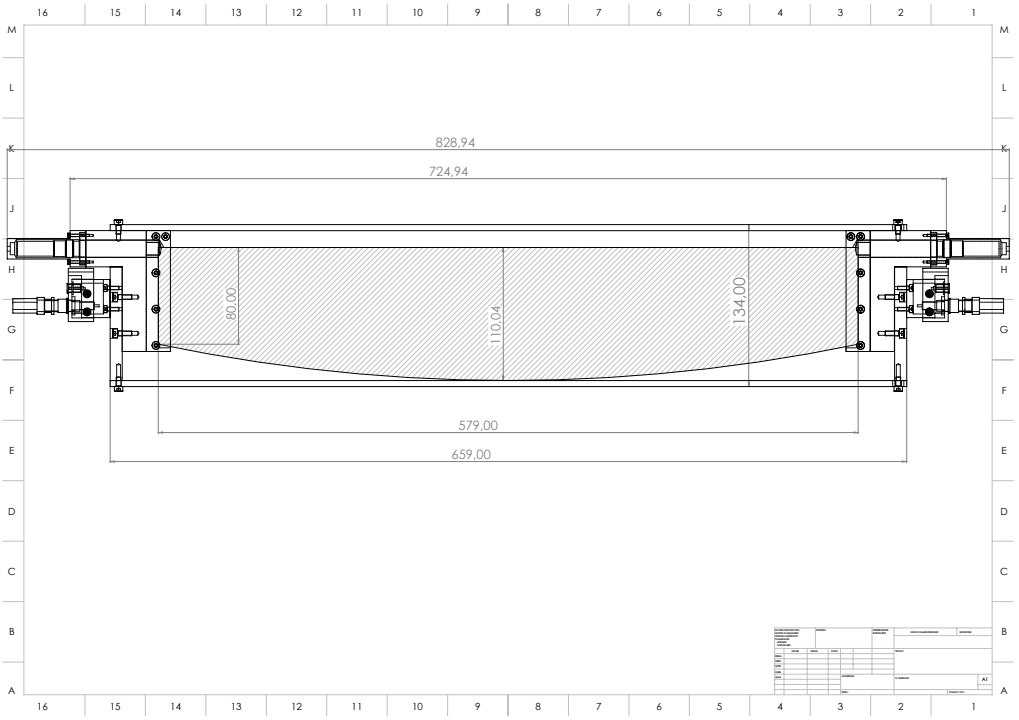

Figure 2.8: Technical drawing of a scintillator inside the aluminium case. The dimensions of each part are expressed in mm.

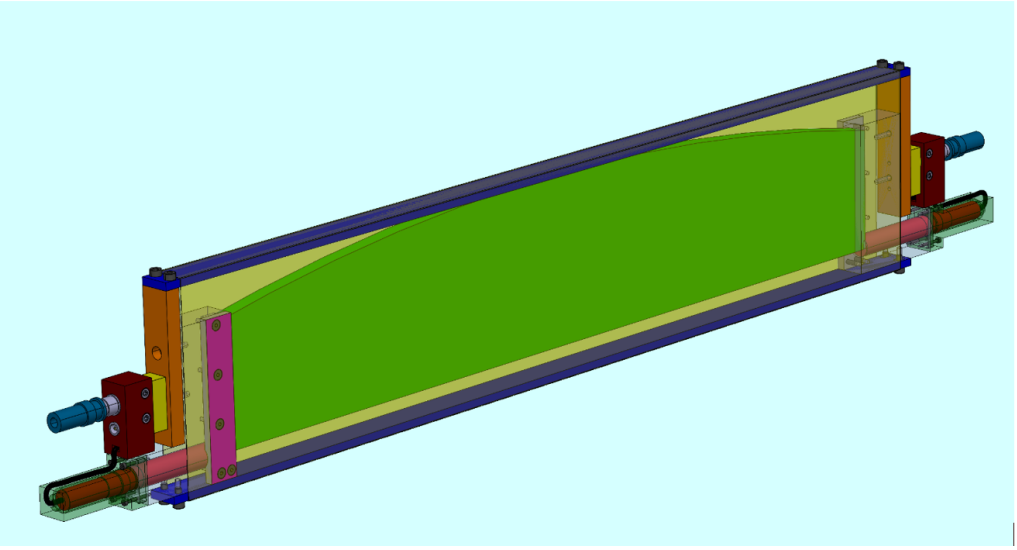

Figure 2.9: 3D model of the aluminium case prototype. The scintillating material is depicted in green. The PMT is colored in red. In this figure, it is possible to visualize the mechanism holding the PMT in contact with the scintillating fibers, located on the straight side of the scintillator. The HV are supplied via the light blue connector, while the output signal to read out through the adjacent LEMO connector.

shifter optical fibers, arranged in two layers of 7 and 8 fibers each, collect the scintillation light produced and guide it to the PTMs located on the two sides of the plane. The optical fibers can be seen in *Fig. 2.10*, depicting a scintillator plane before it was encased in the aluminium.

The planes are covered by light-tight wrapping and enclosed into an aluminium case to reduce noise due to external light. The case also serves as mechanical support to maintain the PMTs window in contact with the optical fiber acting as a light guide, as can be seen in *Figs. 2.12-2.13*. The mechanism relies on the shape of the aluminium parts and a spring to ensure maintaining the PMT in the correct position.

The PMTs are Hamamatsu photomultiplier tubes, shown in *Fig. 2.11*. The model is the H3165-04, employed in the DELPHI ϕ-tagger in the 1995 upgrade to allow higher sensitivity and gain, usable without a preamplifier. These PMTs have a 10 mm diameter, and are 11 cm long.

All the scintillator planes were characterized to find the optimal working point of each PMT. The characterization was done as follows:

- fix the voltage of both PMTs of a scintillator plane used as a reference;
- set the first value of voltage for each of the PMTs of the scintillator to be characterized;

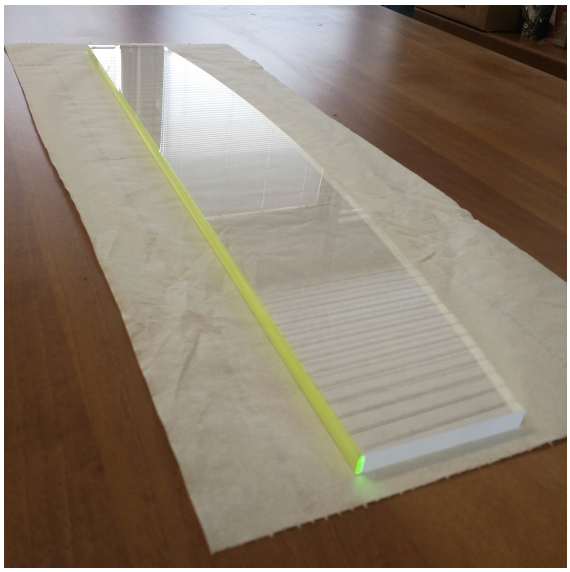

Figure 2.10: Scintillator plane with two layers of optical fibers.

Figure 2.11: Hamamatsu photomultiplier tube H3165-04.

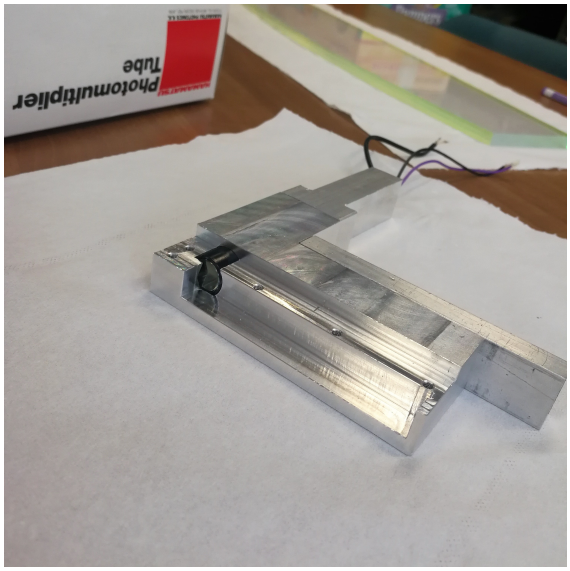

Figure 2.12: PMT inserted into the alumimum support. A spring is inserted inside the casing to maintain the PMT in the correct position.

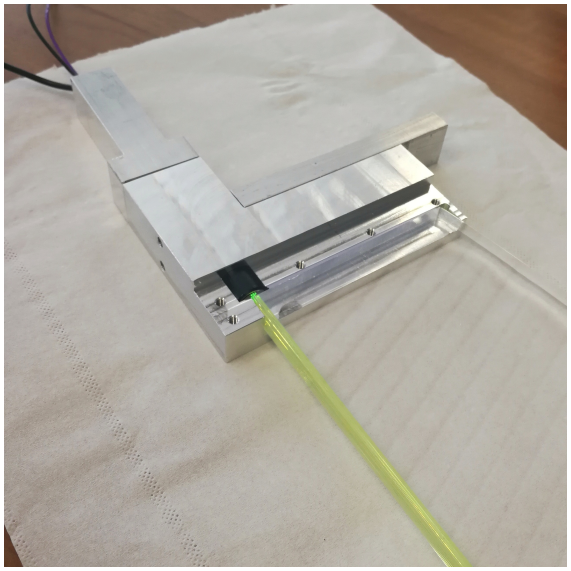

Figure 2.13: Mechanical support to maintain the PMT and the optical fiber in contact.

Photomultiplier	Working Voltage (V)
1L	925
1R	975
2L	900
2R	900
3L	950
3R	925
4L	925
4R	925
5L	975
5R	975
6L	925
6R	900

Photomultiplier	Working Voltage (V)
7L	900
7R	900
8L	950
8R	925
9L	975
9R	975
10L	900
10R	900
11L	900
11R	950
12L	950
12R	900

Table 2.1: Summary table of the PMTs characterization. It reports each PMT the working voltage chosen in V.

- count the coincidence signals of one PMT with the logic `AND` of the two signals coming from the reference plane;
- monitor the events on the single PMT to prevent applying a voltage too high and reaching the discharge region, where the proportionality between light collected and the signal produced is lost;
- modify the voltage applied to the PMTs to study their behavior.

We carried out this procedure for one scintillator plane at the time because, while the CAEN 4-channel HV power supply Mod. N470 could power 3 planes, the CAEN scaler Mod. N1145 only has four channels.

Each counting measure lasted 100 s to have enough events in each measure, and contain the statistical error.

The aim is to find a plateau in the curve to have a stable behavior even in case of fluctuation of the voltage supplied by the High Voltage power supply, which could happen due to random noise or environmental change, i.e. temperature modification. The results of the categorization are summarised in *Tab. 2.1*, while all figures are reported in appendix A.

Even if 12 scintillators were produced, only 9 are used in the telescope setup, as 3, namely numbers 1, 5, and 9 of *Tab. 2.1*, were given to the Padova INFN group.

In the telescope setup, all scintillators are on one plane between the two chambers. This choice aims to cover as many drift cells as possible in both MiniDTs. Given the actual shape of the scintillator planes inside the aluminium casing, the best way to

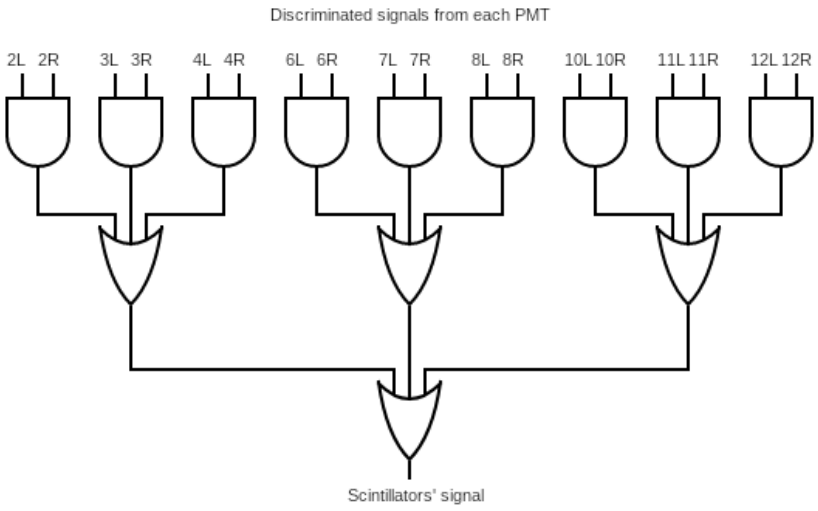

Figure 2.14: Scheme of the logic used to produce the scintillator signal to be forwarded to the NIM-LVDS board and sent to the telescope readout system.

maximize the coverage was to arrange the scintillators in two rows, staggered to fill the dead area given by the gap between the scintillating material and the aluminium casing.

Individual photomultiplier signals are fed into a tree of logic gates to generate a single trigger signal corresponding to a particle crossing the scintillator plane in any position, as illustrated schematically in in *Fig. 2.14*.

First, the signal read from the PMT goes through the CAEN 8 Channels Leading Edge Discriminator (LED) Mod. 840 with a threshold value of 30mV to reduce the noise from each channel. The discriminator output is a NIM signal 800 mV high, 40 ns wide. Then, using CAEN 4-fold Coincidence FAN-IN FAN-OUT Mod. V976 modules, the logic `AND` signal from the two PMTs of the same scintillator is produced. This step is necessary to reduce noise because there are no further layers to compute coincidences in the telescope's current setup.

Lastly, each scintillator signal is sent into a logic `OR` to have the whole layer information. The resulting signal is converted through a custom board from the NIM signal of CAEN logic modules to the LVDS standard, as accepted by the OBDT. We need to thank the Electronics Laboratory of the Bologna section of INFN that designed and produced the NIM-LVDS board. This small board can convert up to four signals and allows using the OBDT for the TDC measurement and the readout of the scintillator signal, together with MiniDTs hits.

Fig. 2.15 shows the prototype assembled for the telescope setup.

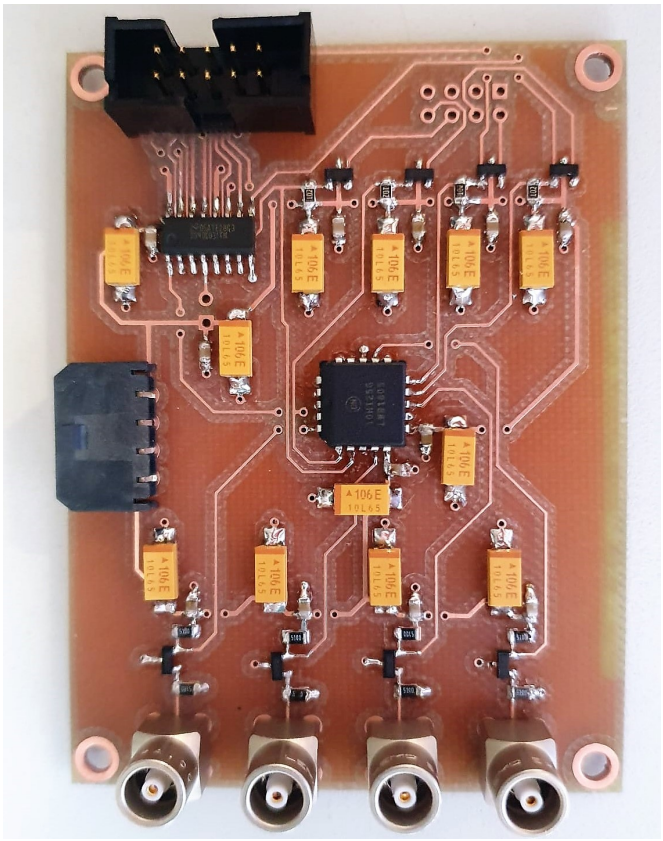

Figure 2.15: NIM-LVDS board used in the telescope setup. The NIM signal input is via the LEMO connectors at the bottom. The LVDS output pins can be seen at the top of the figure.

2.3 Telescope readout setup

2.3.1 Time to Digital Conversion: On Board electronics for Drift Tubes

The first component of the telescope readout electronics is an "On Board electronics for Drift Tubes" (OBDT), shown in *Fig. 2.16*.

It is a new board designed by the Padova CMS group for the Phase-2 upgrade [16] [17] to replace the ROB electronics. The need for a new board stems from the requirement to reduce complexity in the detector and bring to the control room all of the elaborate logic doing the event matching or trigger primitive generation. Moreover, the new design could provide a reduction of up to 60% in power consumption with respect to the present system.

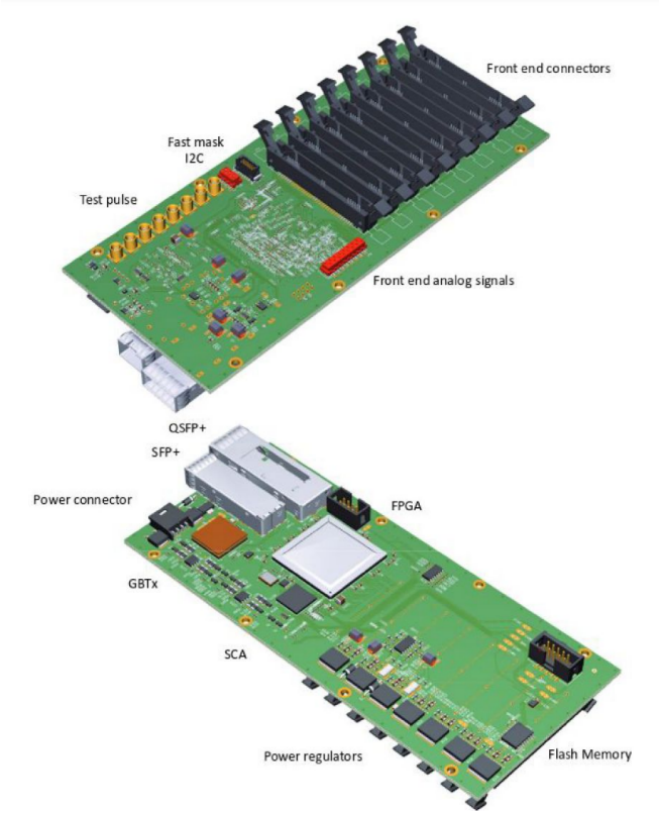

Figure 2.16: OBDT board top (above) and bottom (below) view.

The OBDT receives the analogue signals from the FE electronics and performs the time to digital conversion. The multi-channel TDC is implemented on a radiation-hard FPGA, namely a Microsemi Polarfire MPF300.

In particular, a single OBDT board receives up to 240 LVDS pairs from the DT FE through eight cable connectors. Given that the MiniDTs have only 64 channels each, only 129 pairs are used, considering the scintillators' signal.

The detected transitions are converted to a digital value made of the coarse count in steps of the LHC bunch crossing (BX), which corresponds to 25 ns, and a fine bin size with a least significant bin of 1/30 of a BX, or 0.833 ns.

As can be seen in *Fig. 2.17* , the OBDT receives the slow control and the clock distribution through the GBTx chipset via an SFP+ transceiver.

The board also features a GigaBit Transceiver – Slow Control Adapter (GBT–SCA) ASIC [18] that allows the monitoring and control of additional OBDT capabilities, such as the configuration of the FEBs, including the generation of the analog voltages setting threshold, bias and width.

In the CMS HL-LHC upgrade, the OBDT will forward the digitalized data to the backend electronics to perform the readout and trigger primitive reconstruction.

The board used in the MiniDT telescope is an OBDT version 1, a fully functional prototype also employed in the slice test currently taking data during LHC Run 3.

The OBDTv1 design has already been updated in version 2, whose test is still ongoing at the time of this work. The OBDTv2 is characterized by different power supply management and I/O communications. In particular, the OBDTv2 implements the Low Power GBT (lpGBT) ASIC [19], a newer version of the GBT which is planned to be used in HL-LHC, and VTRX+ optical transceivers [20], radiation-hard devices developed by CERN, in replacement of the commercial SFP+ and QSFP transceivers used in the OBDTv1. Nonetheless, the TDC conversion in the new version uses the same firmware developed for the OBDTv1. When the OBDTv2 will be available, we will update the telescope setup with the new design.

In the MiniDT telescope setup, it communicates with a Xilinx Board described in the following section.

2.3.2 Backend: Xilinx Evaluation Board

The OBDT is controlled and readout by a Xilinx evaluation board, that implements the backend functionalities. A bidirectional optical GBT connection enables clocking, slow control and monitoring of the OBDT, and a further optical link is used for streaming of the TDC data from the OBDT to the backend. A firmware developed by CIEMAT (Madrid, Spain) CMS group for a VC707 Xilinx evaluation board [21], shown in *Fig. 2.19*, based on a Virtex7 FPGA [22], was adapted to implement the needed control and readout features in our setup. Such firmware includes the gigabit transceivers for the communication with the OBDT, IPBus [23] blocks for read/write operations to configuration and status registers, and a Gigabit Ethernet interfaced with the IPBus system. After establishing the desired functionalities, in particular the readout, through the ethernet interface, of a buffer memory receiving OBDT hits, we adapted the firmware

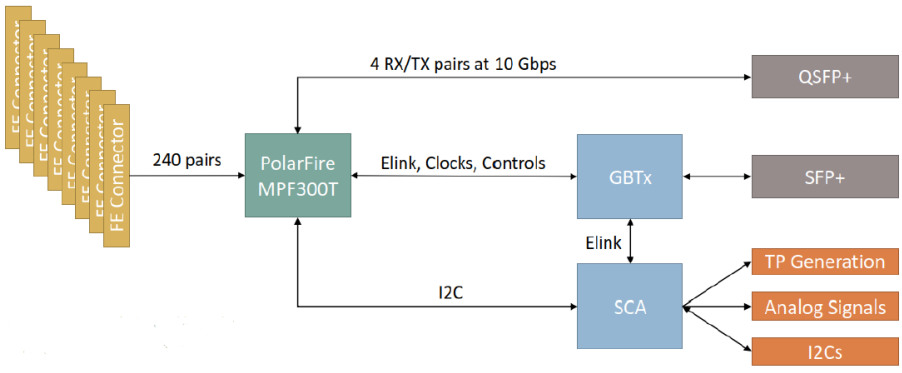

Figure 2.17: OBDT internal components scheme. The main components are a Polarfire FPGA from Microsemi and the GBTx and SCA chips developed at CERN.

to enable its use in a more recent KCU105 board [24], shown in *Fig. 2.18*, that hosts a Kintex Ultrascale FPGA [25]. The Xilinx Kintex and Virtex Ultrascale technologies are the ones that will be used to implement the backend hardware for the CMS Phase2 upgrade.

In our setup, the following interfaces available in the KCU105 are used:

- USB interface: for the FPGA programming from a desktop computer;
- Gigabit Ethernet interface: connected to an ethernet switch, enables the communication between the KCU105 and a desktop computer;
- an FM-S14 mezzanine plugged into an HPC FMC connector, for the optical I/O to/from the OBDT, and clocking.

The FM-S14 mezzanine [26] can host up to 4 SPF/SFP+ transceivers, of which we use two, one for the bidirectional OBDT slow control and clocking link, and one for the stream of TDC hits, and includes a PLL programmable through I2C, whose output is routed to the Kintex FPGA. An IPBus-I2C interface implemented in the firmware allows the PLL output clock frequency to be tuned so that a 120.24 MHz clock (equal to 3 times the 40.08 MHz LHC clock) is generated and used as a reference clock for the GBT transceivers and for all operations that must be synchronised with the OBDT. Within the Kintex firmware, also the LHC timing control signals are emulated, such as the Bunch Crossing Zero (BC0), the Orbit Counter (OC) and the Bunch Crossing Counter (BXC).

The typical operational sequence to start the data acquisition includes:

- programming the KCU105 FPGA through the Xilinx Vivado software;

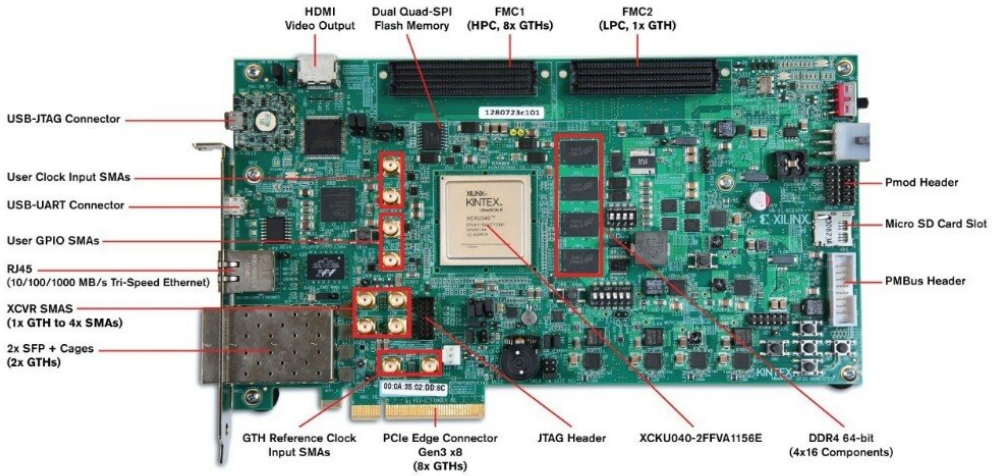

Figure 2.18: Kintex Ultrascale KCU105 board.

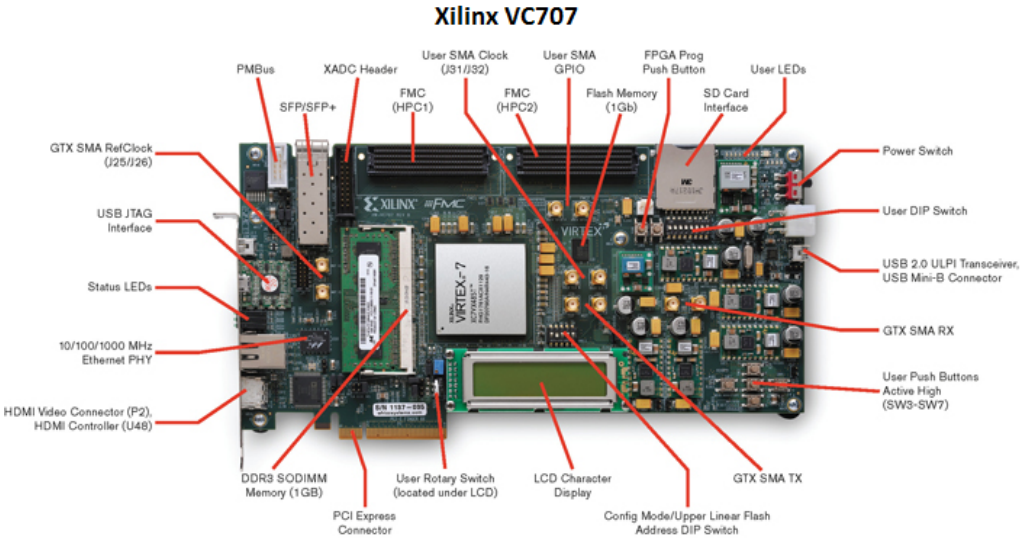

Figure 2.19: Virtex-7 VC707 board.

- checking the ethernet access to the firmware by a command that reads out the firmware version registers;

- configuring the FM-S14 PLL to the desired clock frequency. At this point, a good clock and data I/O between the OBDT and the KCU105 is established;

- configuring the OBDT and checking that it is ready to deliver data.

All operations accessing the KCU105 board via ethernet are developed using a python tool, called dtu.py, based on uHAL libraries [27] and developed by CIEMAT for the control of the DT Slice Test backend system in CMS, which is presently built with ad-hoc firmware deployed on Phase1 μTCA boards [8].

In particular, the configuration of the OBDT includes the setting of masks, to enable/disable individual TDCs. This is important to enable only the channels that we effectively use in the telescope setup (e.g., 64+64 channels for the two MiniDT chambers, plus the scintillator signal) and avoid spurious hits from unused inputs, potentially due to noise, to be added to the data stream.

The data readout is performed with a simple python script, producing a text file. For each hit, one line is written, including:

- Data Acquisition Time, the time elapsed since the beginning of the data taking in seconds;

- Orbit number, the 12 less significant bits of the LHC orbit number emulated by the KCU105;

- OBDT pin, the OBDT channel where the hit was received;

- BX, the bunch crossing associated with the measurement, in each orbit there are 3564 BX;

- TDC fine measurement, the OBDT TDC measurement.

The same script that writes the readout file also takes care of the bookkeeping of the data acquisition history. For each new run, one line is added to a dedicated log file, including:

- the run number;

- the start and end time, including day and hour;

- how many hits were recorded in the run;

- the configuration of the OBDT, i.e., the active channels.

The log file is useful to keep a record of past runs, but it's also used by the readout program itself when it starts to assign the current run number, adding one to the previous one. The data acquisition monitor, described in the next section, also identifies the current run by accessing this log file.

2.4 Data Acquisition Monitor

As part of this project, we developed a program to monitor the data quality and the MiniDTs status during data acquisition [28].

Monitor Operating Principle

The monitor program is a python script that extracts information from the readout file while it is written, performs a simple analysis, and displays the results on a local web page using the Streamlit framework [29], shown in *Fig. 2.20*.

The layout has been developed to display the most important information on a single page, but the web interface is interactive and allows for plots to be zoomed into if more detailed inspection is needed. More details about the displayed plots are given in the next paragraphs.

When the program starts, it opens the latest run file and goes to the end. The basis of the script logic is an endless loop that waits for 30 seconds, reads the newly written data, analyses it to produce and display plots, and then sleeps for another 30 s for new lines to be written in the readout file.

In particular, after waiting, it reads the lines written in the elapsed time and then it associates to each OBDT pin the correspondent MiniDTs channel, layer, and wire numbers. With this information, it builds the occupancy histograms, both per channel and in a 2-dimensional representation of the chamber. The occupancy plots are useful to identify channels with a rate different from what is expected and to locate their position in the chamber.

Whenever the program encounters the scintillators' coincidence signal pin, it proceeds to a basic event building, looking for MiniDTs signals with the same orbit number. If it founds any, the program uses them to build a timebox, i.e. the distribution of the time differences of the chamber hits with respect to the scintillators' signal. As discussed in chapter 3, the width and shape of the timebox are critical for estimating data quality and, when combined with occupancy charts, can aid in diagnosing a wide range of chamber issues.

When finding hits in the chamber associated with a scintillator event, the monitor program produces event display plots for some of those with more than three hits in both chambers. These displays are an effective tool to visualize events in the telescope

Figure 2.20: Monitor webpage.

setup. Only a limited number of the overall events are plotted and shown in a separate window.

Another quantity monitored is the hit rate. This rate is computed using the number of hits read from the readout file and the time difference between the first and the last line read. For the MiniDTs, it's possible to monitor the rate wire by wire. These plots, like the occupancy histograms, are also presented in a 2D format to help visualize the wire location inside the chamber.

In addition, the monitor webpage displays the overall rate of the MiniDTs and the scintillators' plane separately. The value measured from the most recent data is printed on the web page and a plot presents the values computed in the previous 60 iterations, equal to a total time frame of around half an hour, to check rate stability over time.

The plots refresh every 30 s to show the one relative to the latest data read from the telescope.

MiniDT Plots

For each chamber, at every iteration, the following plots are produced using the latest information readout.

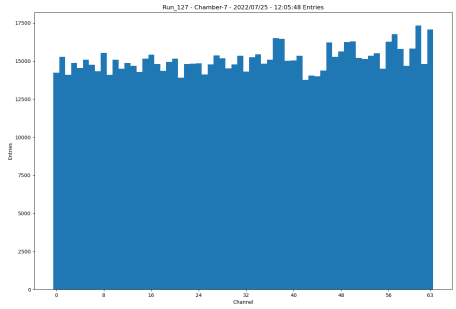

Figure 2.21: Occupancy per channel of a MiniDT.

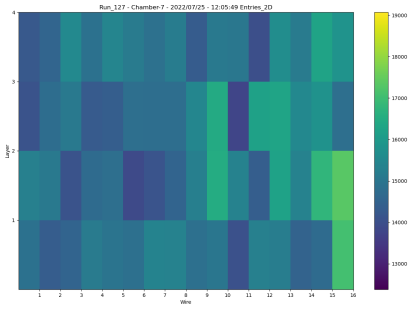

Figure 2.22: 2D occupancy of a MiniDT.

Occupancy

- per channel: the plot shows the cumulative hits in each channel of a MiniDT chamber, numbered from 0 to 63, as can be seen in *Fig. 2.21*;
- 2D: the plot shows the cumulative hits on a 2D map, each rectangle represents one of the chamber cells. The occupancy plot helps in identifying channels with high noise rates or, on the other side, channels with a reduced rate, i.e. *Fig. 2.22*;
- relative to scintillator events, both per channel and 2D: to identify and monitor which channels are covered by the scintillator area. It can also help in identifying problems in the scintillator tiles' behaviour.

The same kinds of plots are also produced after normalising the number of events recorded with respect to the time elapsed. This way, a second set of similar plots is obtained, using the data read in the previous 30 s. These are useful for identifying transient noise sources and visualising their location inside the chamber.

Timebox The plot in *Fig. 2.23* shows the time difference between the scintillator signal and the chamber response. It depends on the drift time of the electrons in the cells and it can help to identify problems in the gas distribution inside the chamber.

As for the occupancy plot, a similar plot shows the time difference between the scintillator signal and the chamber response in the last 30 s of events.

Telescope Plots

The following plots are relative to the single detectors making up the telescope or the overall system. As the other, the program produces them every 30 s adding new data.

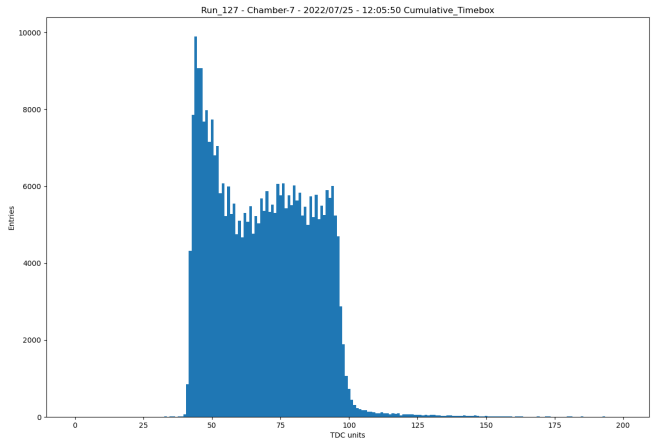

Figure 2.23: Timebox obtained using all events readout while the monitor program is running.

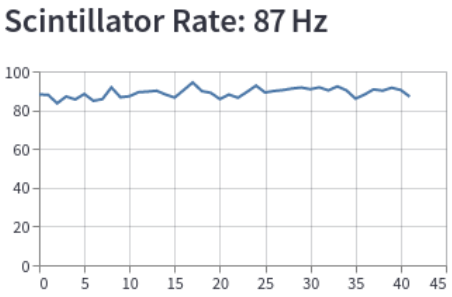

Figure 2.24: Variation of scintillator layer rate over time.

Hit Rate The plot *Fig. 2.24* illustrates the rate values measured in monitor iteration up to half an hour, adding a point at each refresh of the web page, for the two MiniDTs and the scintillators' plane independently.

Event display The plot in *Fig. 2.25* shows a transverse view of the telescope. In each cell, a dot highlights the wire position. The cells that produced the signals are colored to provide a visual representation of the event.

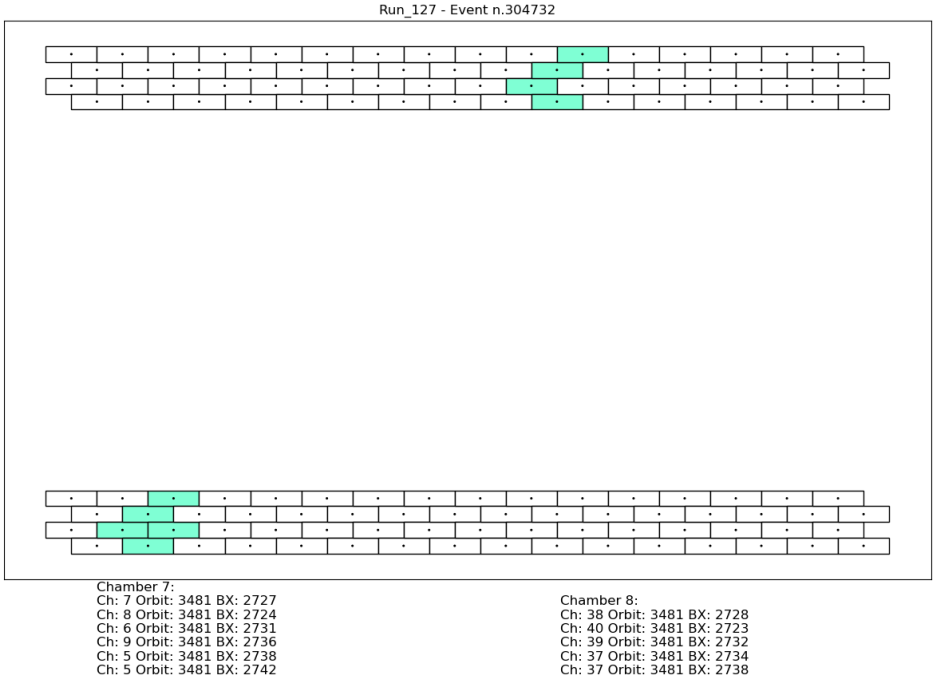

Figure 2.25: Event display of a particle crossing the telescope.

Chapter 3

Offline Data Analysis

Contents

The similarity between the MiniDTs and the actual CMS DT chambers allows using the official CMS offline software (CMSSW) [30] to process the acquired data.

A custom CMSSW producer was implemented, to process MiniDT readout files and produce a ROOT file containing TDC hits with the standard CMS formats. The CMSSW track-segment reconstruction producer is then run and an analyser is finally used to write a ROOT tree that can be processed by the DT Slice Test offline analysis, modified to take into account the MiniDTs.

3.1 Segment Reconstruction and Offline Analysis

Given the similarity with CMS DT chambers, the muon segment reconstruction in the MiniDTs employs the standard CMS DT *local reconstruction* algorithm, which builds track-segments based on information from a single muon chamber.

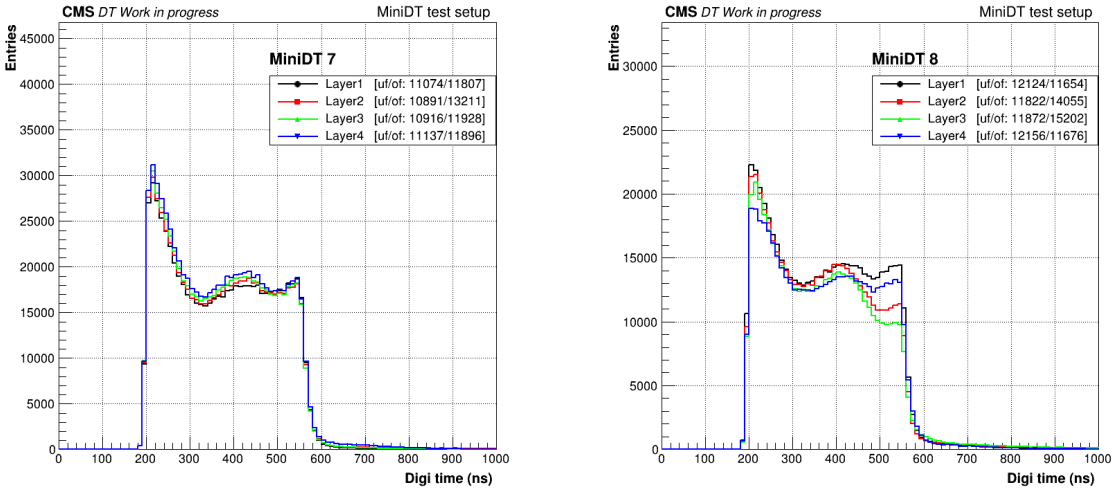

(a) MiniDT 7

(b) MiniDT 8

Figure 3.1: Distribution of the time difference between the scintillators' signal, used as trigger in the offline analysis and the MiniDTs' signals per each layer of the chambers.

In each DT, the hits are reconstructed in the cell using the TDC time measurements, called "digis".

In the telescope, the readout is triggerless, i.e., every signal coming from the chamber is written to the readout file, and the OBDT measures time starting from a simulated, and therefore arbitrary, BC0. Thus, in the case of the MiniDT, the digi producer must use the information of the readout file, i.e., the orbit number, BX count and TDC measurement, to perform the event matching, associating MiniDTs hits with the scintillator time signal. Then, it assigns to each digi a T_{TDC}, which is the difference between the time measurement of the OBDT associated with the hit and the one from the scintillator. This way, in the offline analysis, the scintillator signal reproduces a trigger signal even if the data acquisition does not actually depend on it.

The typical time distribution of hits in a MiniDT, called a "timebox", is reported in *Fig. 3.1.*

The timebox shows the time difference between the trigger signal and the hits recorded in the chambers so ideally, the distribution should be in the interval between 0 ns for particles crossing a cell next to the anodic wire, and $\sim$ 390 ns if the particle crosses the cell near its edge, but it is shifted by a factor called T_{ped}, which takes into account the propagation time of the signal along the anode wire and delays due to cable length, read-out electronics and trigger latency. This parameter is further discussed in section 3.2.1.

The peak at the beginning of the time distribution is due to nonlinear effects in the

avalanche region close to the anodic wire and the delta-ray electrons that pass closer to the wire than the muons.

The tail of the distribution is affected by the feedback electrons. These particles are extracted from the I-beams or the aluminium sheets delimiting the cell by photons emitted during the avalanche process.

We can already notice a difference in behaviour in layers 2 and 3 of MiniDT 8. The lower number of events on the right edge of the timebox suggests problems in the drift field, thus in the efficiency of those layers' cells. More details are reported in section 3.3.1. Furthermore, the slightly reduced number of entries in layer 4 is explained by the occupancy distribution, described in section 3.3.

The underflow and overflow bins of the plots shown in the *Fig. 3.1* contain the digis associated with a scintillator event but are mostly noise. Indeed, the association of scintillator and MiniDTs hits is performed based on the simulated orbit number corresponding to a time window of about 90 μs. In this interval, there can be noise hits or, even with a smaller probability, other events recorded in the MiniDTs. These signals are associated with a given event but do not correspond to the muon detected by the scintillator and, for this reason, fall outside the timebox distribution.

The hit position with respect to the wire is computed as reported in *eq. 3.1*, using the time measurement T_{TDC} corrected with the time pedestal T_{ped}, that is equal to the electrons drift time.

$$x = (T_{TDC} - T_{ped}) \times v_d \tag{3.1}$$

The hits reconstructed by converting the time measurement into a position in the DT cell are called "rechits".

In computing the reconstructed hits, the drift velocity is assumed as a calibration constant parameter, independent of track position and inclination.

Due to the intrinsic ambiguity of the detector, two possible rechits are reconstructed for each TDC measurement because of the left-right ambiguity with respect to the wire. The ambiguity is solved in the segment building stage, exploiting the layers' staggering.

The segment reconstruction is done independently for each MiniDT.

The local pattern recognition algorithm takes the rechits as inputs and considers all possible pairs of hits in different layers as seeds. The algorithm starts from hit pairs with the largest separation and searches for compatible hits in the other layers. The additional hits are included in the segment candidate if they are compatible with the extrapolation in that layer [2]. Segment candidates are then fitted with a straight line and sorted based on the total number of hits associated and the χ^2 value. The latter is computed as the sum of the squares of the hits residuals divided by the hit position error and normalized for the total degrees of freedom of the segment candidate. The reconstruction algorithm chooses for each seed the segment candidate with the maximum number of hits, but at least 3, and best χ^2.

When fitting the segment, an offset common to all hits is added to the distance between the rechit and wire positions, and considered as a free parameter. Hits detected on the left or right side of the wire are shifted in opposite directions. As a result, the fit returns a t_0 parameter, which represents a time shift of all hits belonging to the track. The t_0 is effectively a measurement of the track time, but is also biased by the track impact angle and includes the propagation time of the signals along the anode wires. A further discussion regarding t_0 is in section 3.3.3.

In CMS chambers it is possible to compute the time correction relative to the propagation along the anode wire. Indeed, in CMS DTs at the reconstruction level, having both Φ and θ layers allows for estimating the 3D position of the segments inside the chambers. At this level, the drift time can be corrected by accounting for wire propagation in both views.

In the MiniDTs telescope, this contribution can not be estimated, since we have two SuperLayers with the same orientation, and there is no second view making it impossible to locate the hits along the wires.

However, this contribution is small given the size of the chamber and the wire length of $\sim 0.5\,\text{m}$ that corresponds to $\sim 2.5\,\text{ns}$, and has an average null effect, given the uniform spatial density of cosmic rays.

In the present work, the digis and segments for the offline analysis are produced from the collected data using the code described in [31]. Once configured with the MiniDTs geometry, it produces a .root file in which the digis and segment information are stored for subsequent analysis.

Given the Phase-2 readout architecture, the analysis is done using the code developed for the DT Slice Test demonstrator, presently operating at CMS [32], appropriately modified for the MiniDT case.

This work aims to assess the performance of the single chamber, so each MiniDT is studied separately.

3.2 Calibration

Eq. 3.1 shows that we need to determine T_{ped} and v_d to correctly reconstruct rechits and, subsequently, segments. The values of these two parameters need to be studied since they affect the performance of the telescope system.

3.2.1 Time Pedestals

The drift time is computed by subtracting a time pedestal T_{ped} from the TDC measurement.

In an ideal cell, the timebox distribution shown in *Fig. 3.1* would be a perfect box, starting at $0\,\text{ns}$ for muons passing close to the anode wire and $\sim 390\,\text{ns}$ for the ones

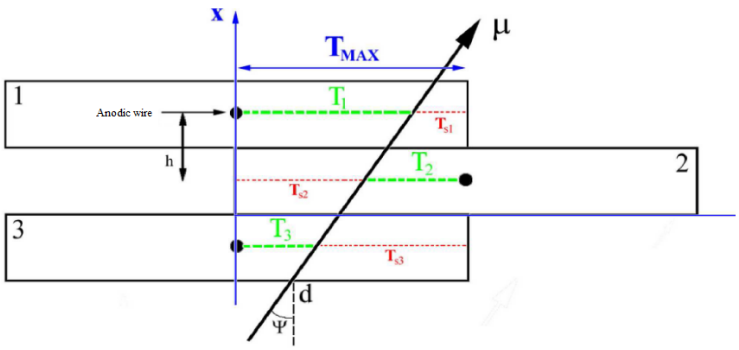

Figure 3.2: Scheme of the mean-timer computation.

crossing the cell close to the cathode. In reality, we need to consider the trigger latency, the time of signals propagating through wires and the delay due to the electronics.

In our set-up, we used cables of the same length for all the FE connectors of both MiniDTs. Thus, the signal propagation is the same for all channels and does not affect the shape of the distribution. The value of T_{ped} can be initially estimated from the rising edge of the timebox distribution. This preliminary assessment allows running an initial version of the local reconstruction that, even if suboptimal, enables more refined calibration studies.

The estimate obtained using the timebox can be corrected by studying the hit position residual. If residuals are computed as described in section 3.3.2, the mean difference between the position extrapolated with a segment and the position of the rechit is different from zero if the time pedestal calibration is not optimal. Thus the time pedestal can be corrected through an iterative process exploiting also information from the t_0 distribution, as discussed in the section 3.2.3.

3.2.2 Drift velocity

In CMS chambers, one of the methods used to compute the drift velocity relies on the mean-timer technique and gives a value of about 54.7 μm/ns.

This method [33] relies on the maximum drift time possible, i.e., the time electrons need to drift through half a cell, being a constant value. This property constrains the sum of the drift times over the hits in a track. In particular, the value of the sum is independent of both the impact position and the direction of the particle.

This technique requires the assumption of a straight trajectory, constant drift velocity in the cells, and constant distance between wire planes.

The mean-timer technique can be applied to tracks with three hits in consecutive planes, as *Fig. 3.2* shows. Then, the following relations hold:

$$\begin{cases} T_1 = d + \frac{5}{2}\, h\, tan(\Psi) \\ T_2 = T_{max} - d - \frac{3}{2}\, h\, tan(\Psi) \\ T_3 = d + \frac{1}{2}\, h\, tan(\Psi) \end{cases} \tag{3.2}$$

where T_n is the drift time of the ionization electrons in the n-th layer, T_{max} is the time needed to drift across half a cell, h is the distance between the anodic wires of two consecutive layers, d is the impact position of the track with respect to the wire, and Ψ is the crossing angle.

Then one can obtain T_{max} as

$$T_{max} = \frac{(T_1 + T_3)}{2} + T_2 \tag{3.3}$$

and the drift velocity knowing the dimension of the cell

$$v_d = \frac{T_{max}}{\text{half cell}}. \tag{3.4}$$

Nevertheless, the mean-timer technique results are influenced by the data quality. For example, the contribution of delta-rays affects the final value. In addition, when trying to derive accurate corrections also exploiting hits in non consecutive layers, the mean-timer algorithm quickly grows in complexity.

For this reason, in the MiniDTs case, we assume the nominal CMS v_d the first time we implement the reconstruction and study the residuals with respect to the distance from the wire. The slope of the distribution gives us information about the drift velocity. Reconstructing the segments with the correct v_d value will result in a slope distribution compatible with zero. Thus, we can fit the profile of the distribution of the residuals as a function of the position with respect to the wire with a linear function to estimate the correction we need for the calibration. The fit is not performed over the whole available range because:

- at small distances, $x < 0.2\,\text{cm}$, the muons pass close to the anodic wire, and due to the avalanche process the the space-time relationship is not linear, as can be also appreciated in the timebox;
- at large x, $x > 2.0\,\text{cm}$, the distribution is influenced by the lower efficiency of the cell's edge.

The results of this procedure are presented in section 3.2.3.

3.2.3 MiniDT Calibration Results

The *Fig. 3.3* shows the residual distribution computed using $v_d = 54.7\,\mu\text{m/ns}$ as the nominal CMS one, and $T_{ped} = 195\,\text{ns}$ for both MiniDTs chosen based on the timebox in *Fig. 3.1*.

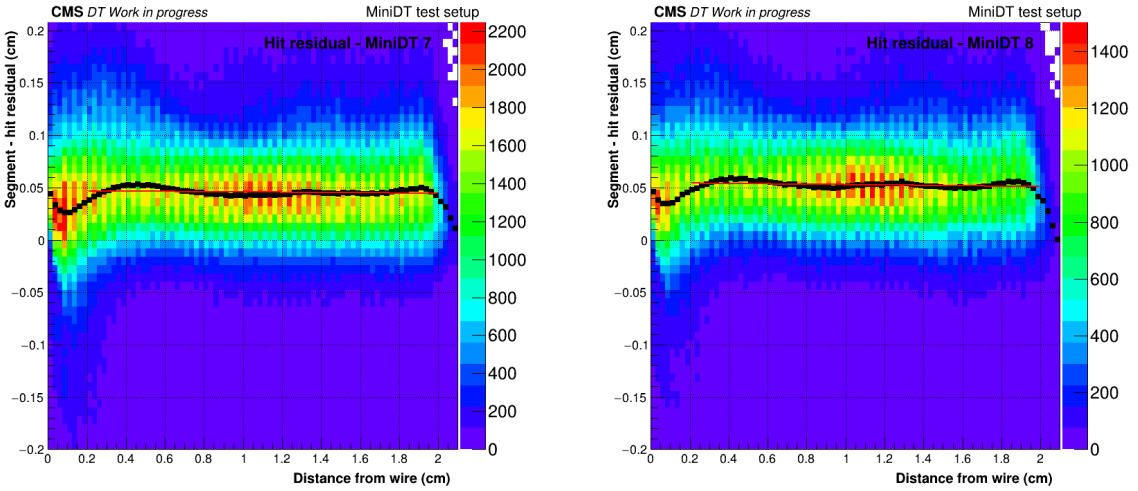

(a) MiniDT 7

(b) MiniDT 8

Figure 3.3: Distribution of the difference, in cm, between the position extrapolated using the segment information and the position of the recorded hit, as a function of the distance from the anodic wire, also expressed in cm. Superimposed in black, is the mean value for each bin. This distribution was obtained before the calibration, using $T_{ped} = 195\,\text{ns}$.

The residuals are plotted as a function of the distance of the hit position from the wire. As explained in the previous sections 3.2.1-3.2.2, this plot is crucial to estimate the calibration parameters of MiniDTs. The black markers identify the profile and allow us to highlight the distribution trend.

For both MiniDTs, we can see that the distributions are shifted towards positive values, indicating a correction needed for $T_{ped} = 195\,\text{ns}$.

However, the profiles are almost horizontal lines indicating that the actual v_d is very close to CMS nominal one. The corrections to the v_d, computed based on the linear fit slopes, result more than one order of magnitude smaller than the resolution of the segment-hit residuals, discussed in section 1.6, therefore v_d was not changed.

Based on the fit results, new reconstruction was performed with the updated calibration constants.

The last correction to the value of the time pedestal was done using the t_0 plots, described in section 3.3.3. The final results are $T_{ped-MiniDT\,7} = 187.75\,\text{ns}$ and $T_{ped-MiniDT\,8} = 186.51\,\text{ns}$.

Fig. 3.4 shows the residual distribution after the calibration. We can appreciate how the mean of the residuals' profiles is much closer to what is expected.

Concerning T_{ped}, the distribution is still not perfectly centred around zero, as illustrated in *Fig. 3.12* and discussed in section 3.3.2. This effect depends on the asymmetry

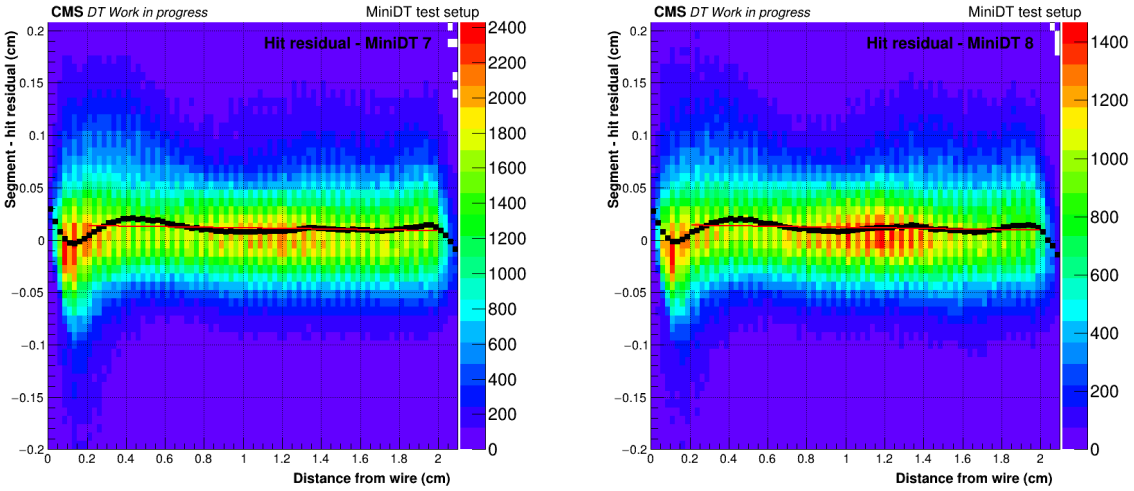

(a) MiniDT 7

(b) MiniDT 8

Figure 3.4: Distribution of the residuals after the calibration. Superimposed in black, is the mean value for each bin. The left one (a) refers to MiniDT 7, on the right (b) to MiniDT 8. This distribution was obtained after the calibration, using $T_{ped-MiniDT\,7} = 187.75\,\text{ns}$ and $T_{ped-MiniDT\,8} = 186.51\,\text{ns}$.

in the residual, mostly due to the contribution of delta-rays and arises from the impossibility of performing quality cuts on the segments to reduce the delta-ray contribution since to compute residuals we need hits in all layers of a MiniDT.

This effect could be minimized by studying the Gaussian fit of the peak in each bin instead of considering the mean value, as in the profile. This way, the inaccuracy in the results from the linear fit used to validate the v_d should also be reduced.

Anyway, the purpose of the calibration is to centre the residual mean on zero, and this was achieved, as can be seen in *Fig. 3.12*.

In the case of MiniDT 8, the very different behaviour of the four layers, further discussed in section 3.3.1, makes the T_{ped} and v_d calibration intrinsically suboptimal as the reconstruction code allows for a single value v_d per SuperLayer.

3.3 MiniDT Performance

The analysis result allowed us to estimate the efficiency and resolution of each MiniDT in the telescope system.

The occupancy of the two chambers, shown in *Fig. 3.5*, is different due to their different position with respect to the scintillators' layer. In particular, the MiniDT 7

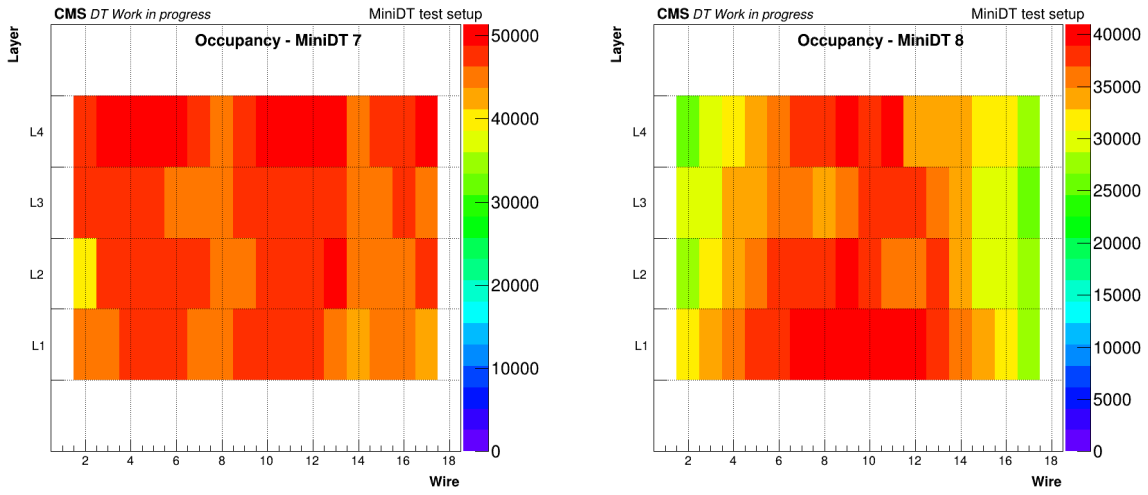

(a) MiniDT 7

(b) MiniDT 8

Figure 3.5: Occupancy of digis in the MiniDTs as a function of layer and wire.

is closer, as it serves as mechanical support to the scintillators themselves, while the MiniDT 8 is more distant, as it is located directly above at a distance of $\sim 28.3\,\text{cm}$. This disposition results in the MiniDT 7 being evenly populated, while fewer hits associated with a scintillator signal are produced in cells at MiniDT 8 sides.

When considering the occupancy of hits associated to segments shown in *Fig. 3.6*, we can identify a new feature. In both chambers, the first cell in layers 2 and 4 and the last cell in layers 1 and 4 have a reduced number of entries. The chamber geometry is responsible for this effect since, as said in section 1.1.1 and as can be visualized in *Fig. 2.25* , the layers are staggered by half a cell. The reduced occupancy of these cells depends on the fact that is unlikely to reconstruct in those cells a segment having at least three hits.

3.3.1 Hit efficiency

The hit efficiency of each MiniDT cell is estimated using segments to extrapolate to cells and check if there is a digi in the cell expected from the extrapolation using the fit result.

For this reason, the efficiency is studied one layer at a time. First, the algorithm checks if the segment has three hits in the remaining layers. Then, using the straight-line fit, one can expect in which cell the fourth one should be. The cell is then considered efficient if there is a digi, inefficient otherwise.

To consider the edge effects, the algorithms considers also the neighbouring cell in this computation.

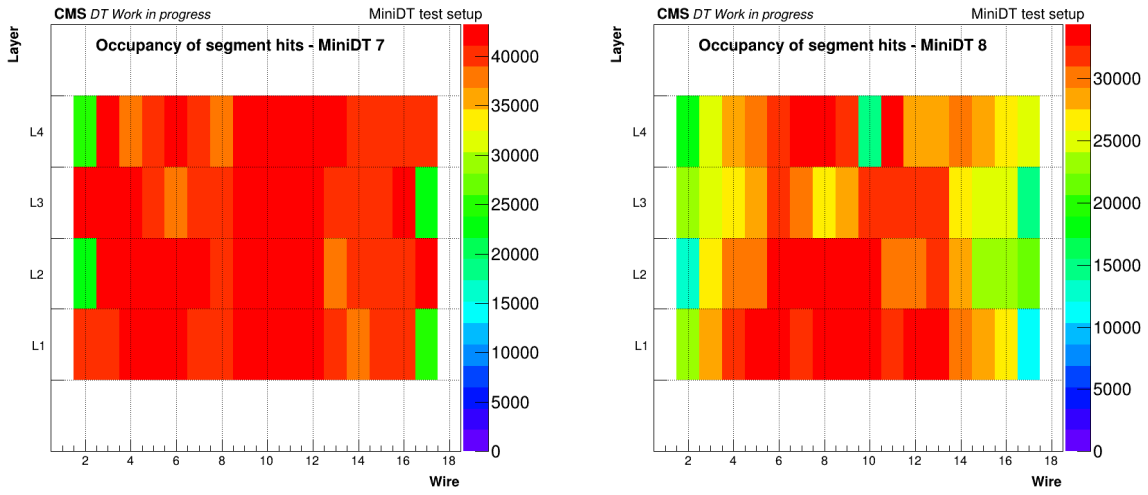

(a) MiniDT 7

(b) MiniDT 8

Figure 3.6: Occupancy computed with segments in the MiniDTs as a function of layer and wire.

For each cell, the efficiency is computed as:

$$\epsilon_{cell} = \frac{\Sigma \,\text{digi in cell} \,\pm 1}{\Sigma \,\text{segment extrapolated in cell} \,\pm 1} \tag{3.5}$$

Fig. 3.7 shows the efficiencies obtained for the two MiniDTs.

All channels on the MiniDT 7 have an efficiency of more than 95%, as seen in the 1D plot in *Fig. 3.8a*. The only exceptions are wires 5 (L3W5) and 6 (L3W6) of layer 3, which however retain an efficiency of 90%.

This behaviour was further investigated by studying the efficiency as a function of the distance from the wire inside a cell, as this information helps in investigating the uniformity of the cell response. In *Fig. 3.9* are reported the average values for each layer, while the specific behaviour of L3W5 and L3W6 can be seen in *Fig. 3.10*. It is appreciable how in both chambers the efficiency is strongly asymmetric, on the right for L3W5 and the left for L3W6. Both lose efficiency in the region $1.5\,\text{cm} < x < 2\,\text{cm}$ from the anode wire, in which the efficiency is $\sim 20\%$. This effect can likely be explained by a misplaced spring supplying the HV to the cathodes located on the I-beam that separates two contiguous cells, as described in section 1.1.2. A faulty connection results in a deviation from the nominal drift field and a local difference in response of the cell. We will address this issue by opening the MiniDT enclosure from the HV side and ensuring every cathode receives the power correctly.

MiniDT 8 instead shows a higher number of channels with reduced efficiency, even if

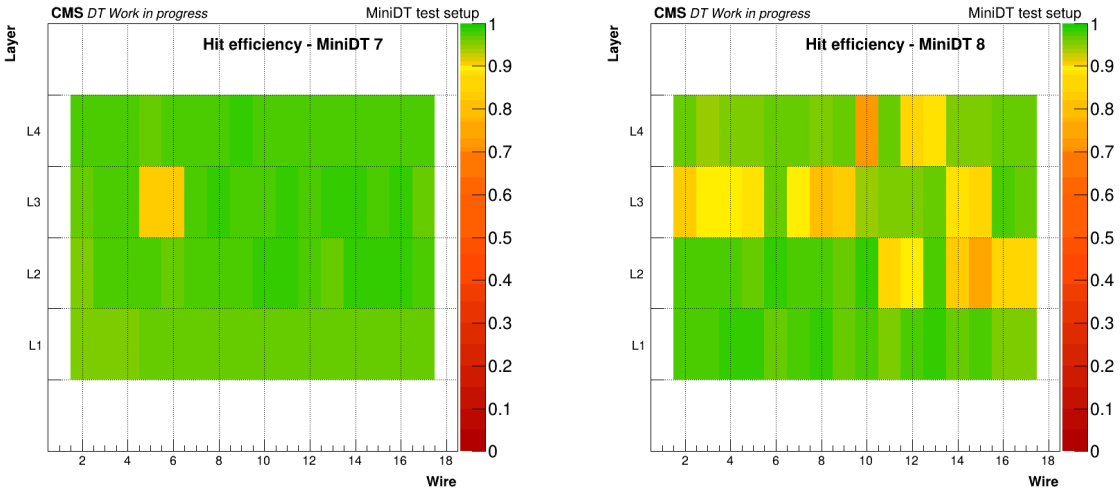

(a) MiniDT 7 (b) MiniDT 8

Figure 3.7: Efficiency of reconstructed segments in the MiniDTs as a function of layer and wire.

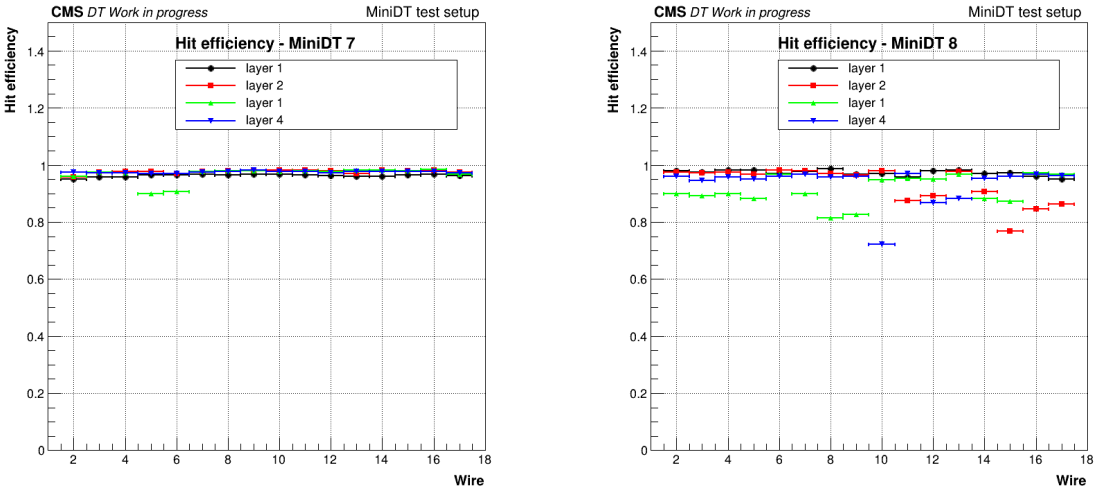

(a) MiniDT 7 (b) MiniDT 8

Figure 3.8: Distribution of the efficiency as a function of the wire per layer.

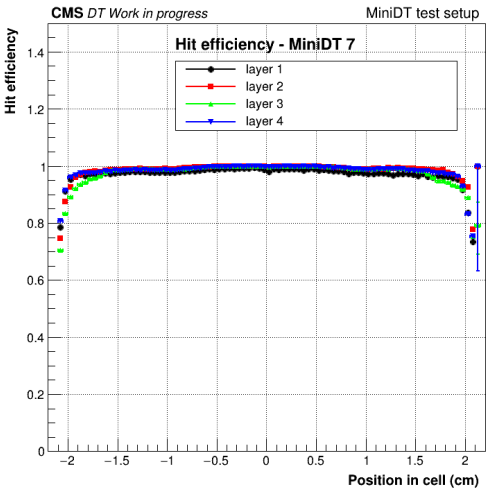

(a) MiniDT 7

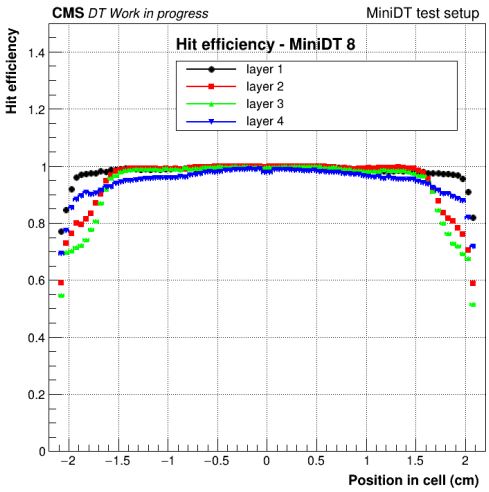

(b) MiniDT 8

Figure 3.9: Efficiency inside a cell as a function of the distance from the anodic wire per layer.

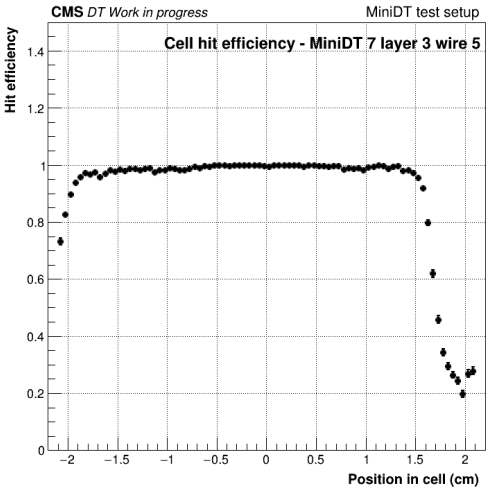

(a) Layer 3 Wire 5

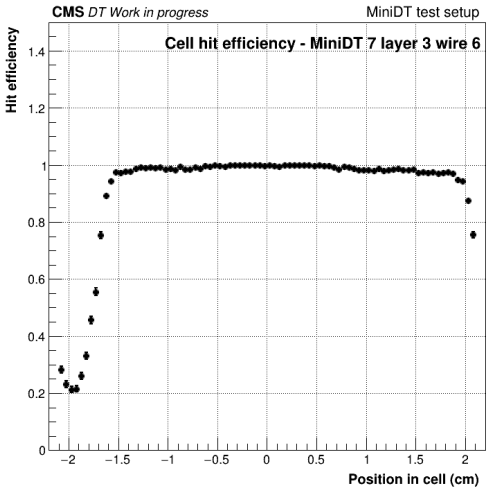

(b) Layer 3 Wire 6

Figure 3.10: Efficiency as a function of the distance from the anodic wire per cell.

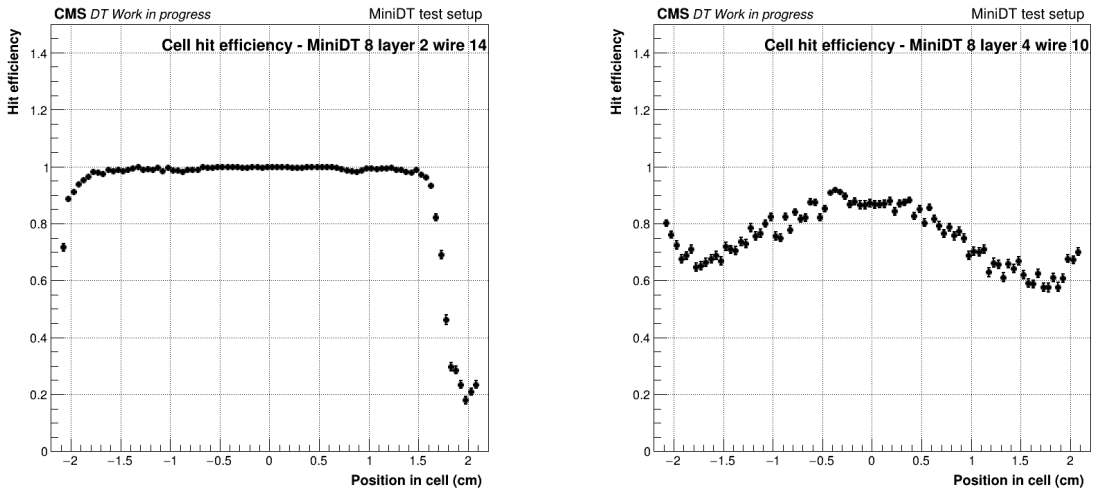

(a) Layer 2 Wire 14

(b) Layer 4 wire 10

Figure 3.11: Efficiency as a function of the distance from the anodic wire per cell.

the great majority has an $\epsilon_{cell} > 95\%$ also in this case, as the *Fig. 3.9b* shows. Similarly to MiniDT 7, we analyzed the behaviour of the inefficient cells by looking at the efficiency as a function of the distance from the wire. While the average value per layer of MiniDT 7 showed behaviour consistent with properly working drift cells, for MiniDT 8, given the larger number of channels involved, the deviations from the correct shape can be already appreciated in layers 2 and 3.

By analyzing the behaviour of the single cells we identified channels with a shape similar to the MiniDT 7's less efficient cell as L2W14, whose efficiency distribution is shown in *Fig. 3.11a*. However, there is also a small number of cells showing a shape that can not be explained by unconnected cathodes, an example is L4W10 as shown in *Fig. 3.11b*. These channels require further investigation.

3.3.2 Space resolution

The spatial resolution is assessed using the width of the distribution of the residual between the reconstructed hit position, and the position estimated by extrapolating the segment.

The resolution could be computed from the residual width by applying standard analytical factors calculated from the "hat matrix" that relates the residuals from a fit to the fitted measurements, and hence the widths of the residual distributions to the intrinsic resolution of the measurements [12].

For the purpose of this work, the resolution of the MiniDT telescope was estimated

using only the residual distribution, neglecting the additional uncertainty relative to the segment fit.

Similarly to the hit efficiency, to estimate the spatial resolution of a hit in a layer, one considers the segments with 3 hits in the other three layers of the MiniDT, extrapolates the fit and computes the residual.

However, a factor ± 1 multiplies the residual based on the position of the hit in the cell. In particular, if the hit is in the left part of the cell, the difference is multiplied by -1. This factor was added to highlight those effects, such as the delta-ray contribution, that affect the distribution but have a null mean. Hence, without this correction, the hit residual would always be centred around zero and we would lose the information needed for the time pedestal calibration.

Fig. 3.12 shows the results of the residual computation. This distribution is the projection on the y-axis of the ones shown in the section 3.2.3. In these plots is easier to see how the Gaussian core of distribution is centred around zero after the calibration procedure.

The asymmetry in the right part of the distribution is the already mentioned contribution of delta-rays, and its position can be explained with the multiplicative factor discussed above.

Indeed, a delta-ray can be acquired in place of the muon signal if it is closer to the wire than the muon itself. This results in a positive residual since the expected distance is larger than the measured one. On the other side of the cell, the residual would be negative but thanks to the multiplicative factor modifying the sign, the contribution on the left side adds to the right one.

Fig. 3.13 shows the distribution and the numerical results of the fit for each layer. It is possible to see that also in this case MiniDT 8 suffers the lower statistic and the inhomogeneity in the different layers given from the inefficient channels mainly localized in layer 3.

3.3.3 Time resolution

The time resolution of the telescope based on MiniDTs can be estimated by studying the distribution of arrival times of muon tracks, called t_0, using the reconstructed segments. This information can be treated as a free parameter in the fit as discussed in section 3.1.

The distribution of the t_0 values obtained is shown in *Fig. 3.14*.

The reduced number of entries for MiniDT 8 depends also in this case on the reduced efficiency.

The observed resolution is not too different from what can be expected in CMS DTs [34].

We must consider that the MiniDTs are studied singularly, and the t_0 value is computed with 4-hit segments that are more prone to delta-ray contribution and make impossible any quality cut. Instead in CMS, the t_0 value is computed using both Φ SLs,

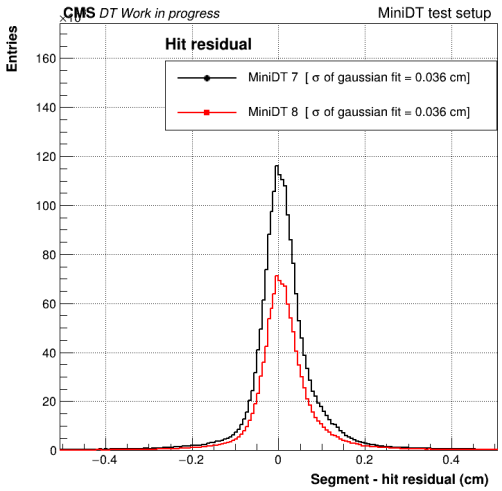

Figure 3.12: Distribution of the difference, in cm, between the position extrapolated using the segment information and the position of the recorded hit.

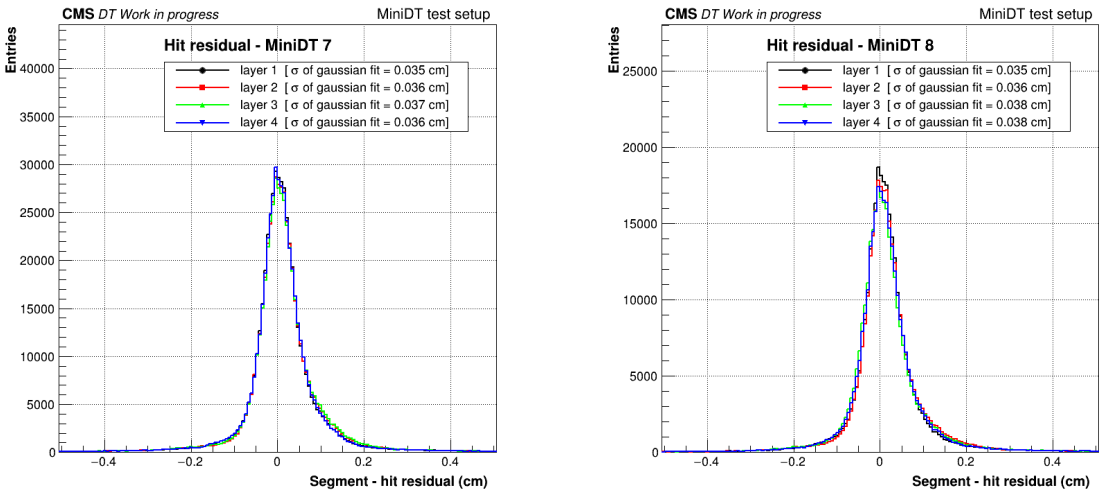

(a) MiniDT 7 (b) MiniDT 8

Figure 3.13: Distribution of the difference, in cm, between the position extrapolated using the segment information and the position of the recorded hit per layer.

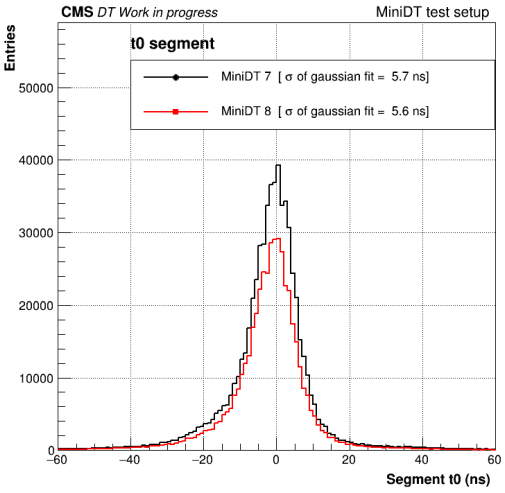

Figure 3.14: Distribution of the t_0 value obtained from the segments' analysis.

since it is possible to select the segments with up to 8-hits to achieve better resolution. Moreover, the information from other detectors can be exploited to select high-quality tracks and implement corrections.

Thus, while DT chambers can achieve a single hit resolution of ~ 4.5 ns, in the current telescope configuration a resolution of ~ 6 ns is reasonable.

In addition to the intrinsic MiniDT time resolution, other contributions affect the observed value, the main ones being the jitter of the scintillator signal, and the time of signal propagation along the chamber wires.

As already discussed in section 3.1, in the MiniDTs case we could not account for the propagation time of the signal along the wire, since we do not have a θ SL. This contribution, of the order of ~ 0.4 ns, affects the final resolution, even if to a smaller extent compared to CMS DTs, given the shorter wire of the cells.

The contribution from the jitter of the scintillator signal was not studied as a part of this thesis work, but we set a lower limit to its value using the coincidence of two tiles. We estimated it to be ~ 2.3 ns. However, the measurement was made using the discriminated NIM signals, thus not including the contribution of the rest of the readout electronics.

The uncertainties of the intrinsic MiniDT resolution, the propagation along the wire and the jitter of scintillator signal are independent so the final resolution is their squared sum. To conclude, further studies of the additional contributions are needed in order to reach a more detailed understanding of the intrinsic time resolution of the telescope.

Conclusions and Future Developments

This thesis work focused on constructing and commissioning a cosmic-rays telescope using two MiniDTs, reduced-size replicas of CMS DT chambers. The telescope is instrumented with the Phase-2 readout system prototypes.

The work started at the INFN national laboratories of Legnaro, where the MiniDTs were manually assembled using spare material from the original chambers. The two MiniDTs were brought in Bologna and connected to a prototype of the On Board electronics for Drift Tubes (OBDT), the time-to-digital conversion board designed for the Phase-2 upgrade.

The telescope system is completed by a scintillator plane, located between the two MiniDTs and made of 9 scintillating tiles, enclosed in aluminium and read by two photomultipliers each. The scintillator plane signal, obtained using NIM logic modules, allows for independent detection of a particle crossing the telescope. In order to read out this signal together with the MiniDTs hits, a custom NIM-to-LVDS conversion board was designed and produced in Bologna.

The OBDT forwards digitised hits to a KCU105 Xilinx evaluation board, which hosts a firmware derived from the one in use in the DT Phase-2 Slice Test demonstrator, developed at CIEMAT. The readout system is completely triggerless: all hits produced by the OBDT are streamed to the KCU105, which is connected to a computer running a python program that writes the data to disk. The matching between the scintillator signal and MiniDT hits is performed within the software programs used for online monitoring and muon track reconstruction.

In order to verify the data quality during the data acquisition, we developed a monitoring program that allows us to see in real-time the occupancy and rate of the chambers.

In addition, it performs a basic event reconstruction using the scintillator signal to compute and show the the distribution of the time difference between the scintillator plane and the MiniDTs signals. The overall shape of this plot helps in identifying problems linked to the drift of electrons inside the chamber, thus related to the shape of the electric field inside the cell volume.

The offline analysis instead relies on the CMS software to produce the ROOT trees

and analyze them. We customized the code produced to analyze the data of the ongoing Slice Test to account for the reduced size of the MiniDTs and the different formats of the readout file.

The calibration parameters needed to reconstruct track segments in the chambers are the average drift velocity of ionisation electrons within the cell volume and the time pedestals, corresponding to the signal arrival time measured for electrons released very close to the anode wire. The estimated drift velocity resulted compatible with the CMS reference one of $v_d = 54.7\,\mu$m/ns for both chambers, and we obtained time pedestal values of $T_{ped-MiniDT\,7} = 187.75\,$ns and $T_{ped-MiniDT\,8} = 186.51\,$ns.

The offline analysis allowed us to measure the overall detection efficiency of both chambers. MiniDT 7 has an efficiency of $\geq 95\%$ in all cells, except for two of them, while we identified many inefficient channels in MiniDT 8 that require further studies to be fully understood and solved.

Nevertheless, we could estimate for both chambers a spatial resolution around 360 μm and a time resolution of $\sim 5.6\,$ns.

The next step must be to address the inefficiencies. Some of the problems are understood as being due to unconnected cathodes, and in order to fix them we will open the chamber HV side to adjust the position of the spring supplying the cathodes with the high voltage. Further studies must be carried out on MiniDT 8 to better understand some of the issues, which clearly are of a different kind.

Another important measurement that can improve our understanding of the performance of the MiniDTs is related to the uncertainty in the timing of the scintillator layer signal, which is included in the chamber resolution measurement in present analysis.

Once both MiniDTs will be properly working, a further step to improve the telescope performance would be to study the alignment of the MiniDTs with respect to each other and try to further develop the offline analysis to combine the information of the segment reconstructed in both chambers.

In addition, one could rotate by 90° one of the two MiniDTs to perform a 3D reconstruction of the tracks, enabling also the capability to correct for anodic wire propagation time, which would result in an improvement of the time resolution.

However, as a result of this thesis work, the MiniDT telescope is now operational and its performance can be constantly monitored, thus it can be now used for local tests of CMS Phase-2 upgrade electronics. This enables the capability to develop and test new tools and methods to perform online track identification and reconstruction that can be exploited in the CMS Muon trigger system. Moreover, the MiniDTs could be operated together with other detectors being developed in the Bologna laboratories to assess their performance.

Appendix A

Appendix: PMTs characterization figures

A high voltage scan was performed to characterise the photomultipliers used in the scintillator plane of the telescope, and the results are reported in this Appendix.

Each counting measure lasted 100 s. The discriminator threshold was set at 30 mV. *Fig. A.1* shows the logic used during the data acquisition.

Error bars are present in all the plots reported, for the single counting they are not always visible since are smaller that the marker size, given the large number of counting for each photomultiplier even at the lower voltages under study, and the large variability from lower to higher voltages.

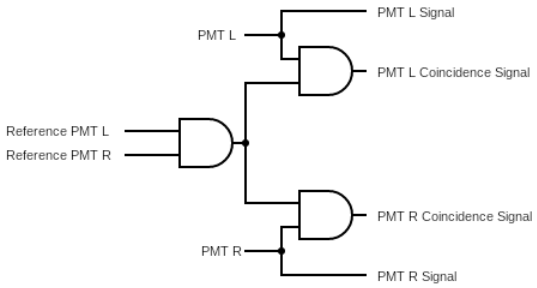

Figure A.1: Schematic representation of the logic used to characterize the PMTs. The coincidence signal is made using the `AND` of the single PMT with the reference plane signal, which in turn is the end of the two PMTs instrumenting the same scintillator.

Scintillator 1

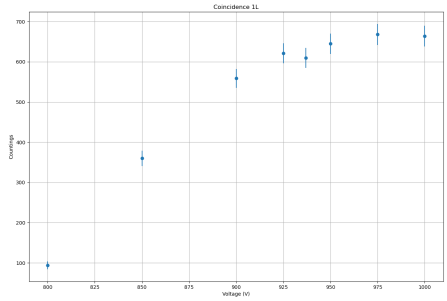

Figure A.2: Coincidence signals as a function of the applied voltage for PMT 1L.

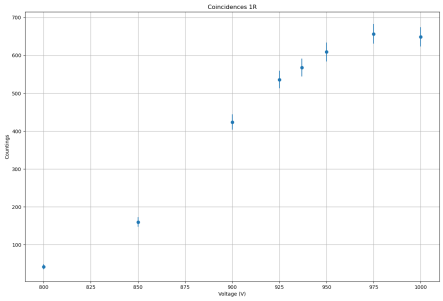

Figure A.3: Coincidence signals as a function of the applied voltage for PMT 1R.

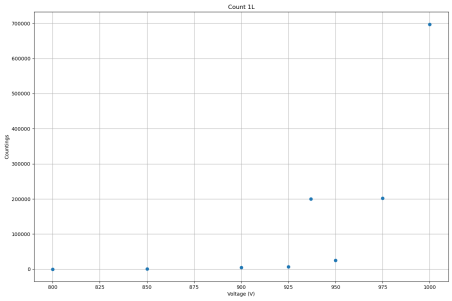

Figure A.4: Counting measure as a function of the applied voltage of PMT 1L.

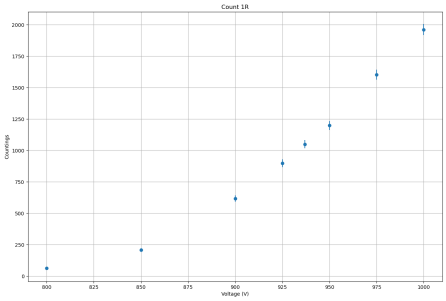

Figure A.5: Counting measure as a function of the applied voltage of PMT 1R.

Scintillator 2

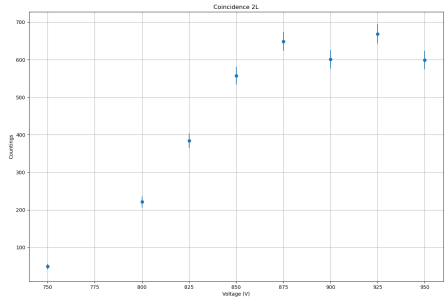

Figure A.6: Coincidence signals as a function of the applied voltage for PMT 2L.

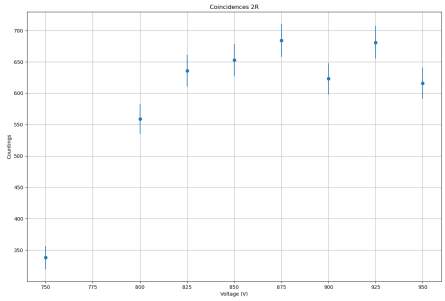

Figure A.7: Coincidence signals as a function of the applied voltage for PMT 2R.

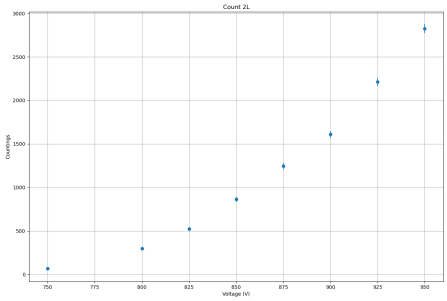

Figure A.8: Counting measure as a function of the applied voltage of PMT 2L.

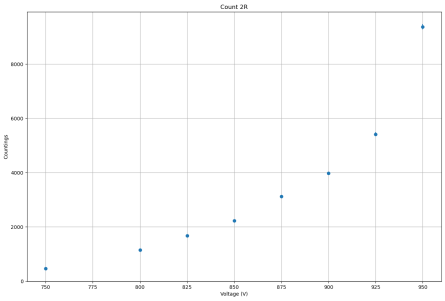

Figure A.9: Counting measure as a function of the applied voltage of PMT 2R.

Scintillator 3

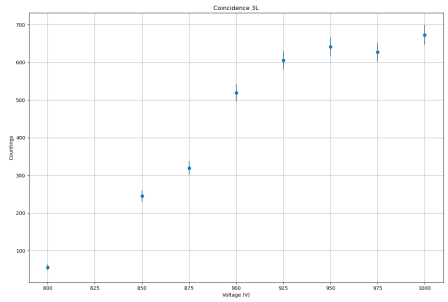

Figure A.10: Coincidence signals as a function of the applied voltage for PMT 3L.

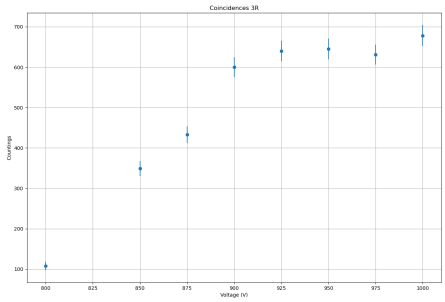

Figure A.11: Coincidence signals as a function of the applied voltage for PMT 3R.

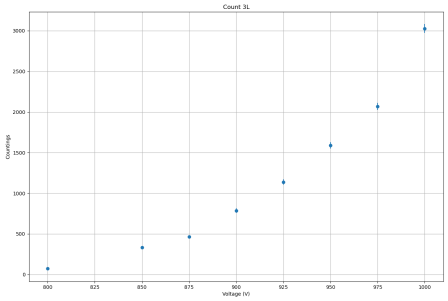

Figure A.12: Counting measure as a function of the applied voltage of PMT 3L.

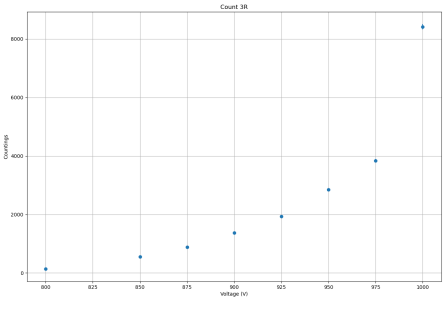

Figure A.13: Counting measure as a function of the applied voltage of PMT 3R.

Scintillator 4

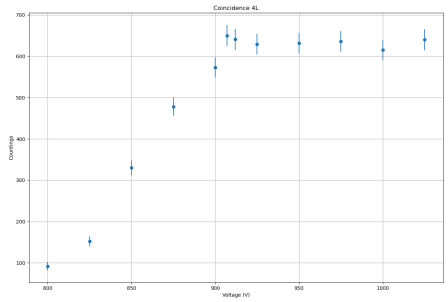

Figure A.14: Coincidence signals as a function of the applied voltage for PMT 4L.

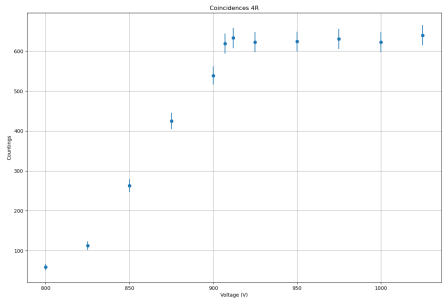

Figure A.15: Coincidence signals as a function of the applied voltage for PMT 4R.

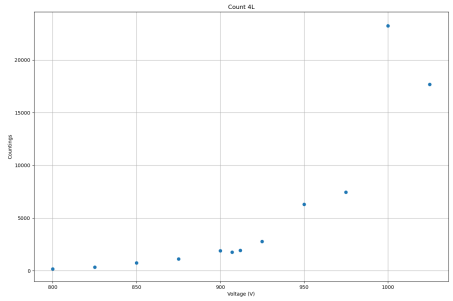

Figure A.16: Counting measure as a function of the applied voltage of PMT 4L.

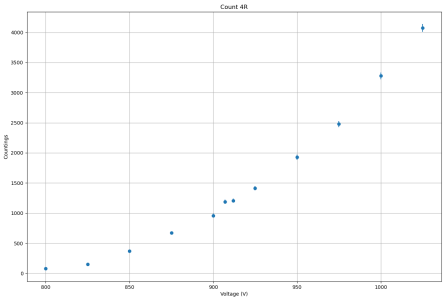

Figure A.17: Counting measure as a function of the applied voltage of PMT 4R.

Scintillator 5

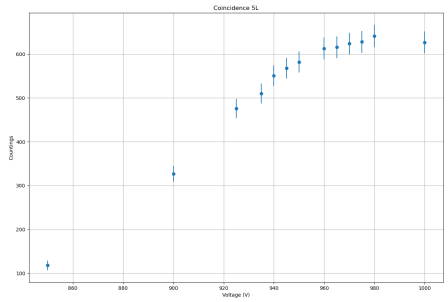

Figure A.18: Coincidence signals as a function of the applied voltage for PMT 5L.

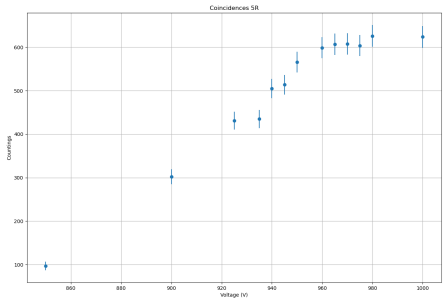

Figure A.19: Coincidence signals as a function of the applied voltage for PMT 5R.

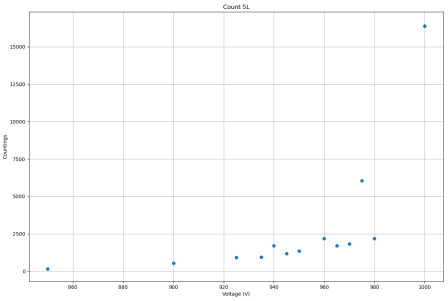

Figure A.20: Counting measure as a function of the applied voltage of PMT 5L.

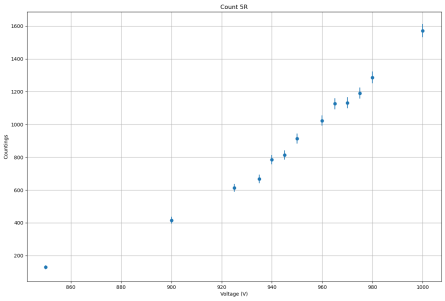

Figure A.21: Counting measure as a function of the applied voltage of PMT 5R.

Scintillator 6

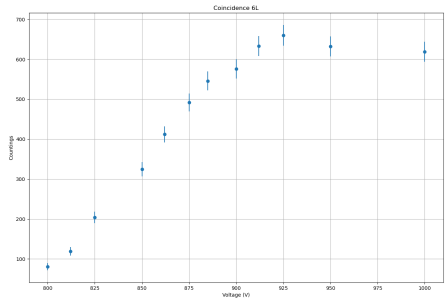

Figure A.22: Coincidence signals as a function of the applied voltage for PMT 6L.

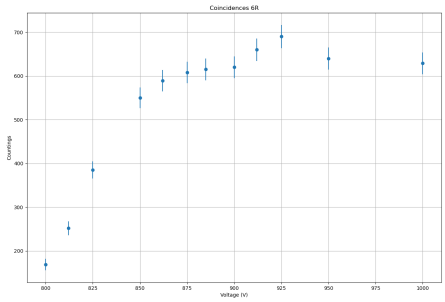

Figure A.23: Coincidence signals as a function of the applied voltage for PMT 6R.

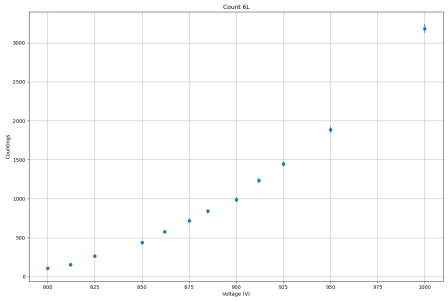

Figure A.24: Counting measure as a function of the applied voltage of PMT 6L.

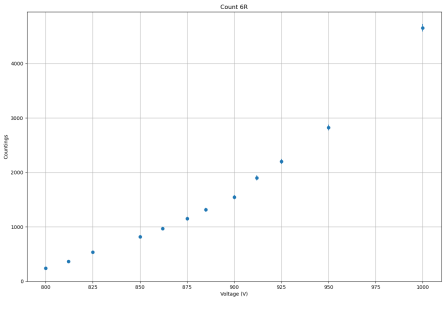

Figure A.25: Counting measure as a function of the applied voltage of PMT 6R.

Scintillator 7

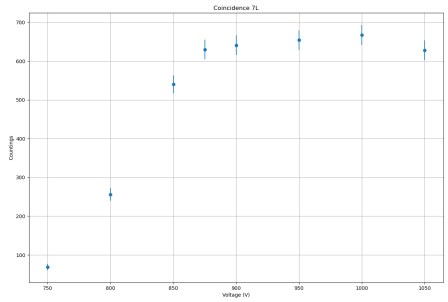

Figure A.26: Coincidence signals as a function of the applied voltage for PMT 7L.

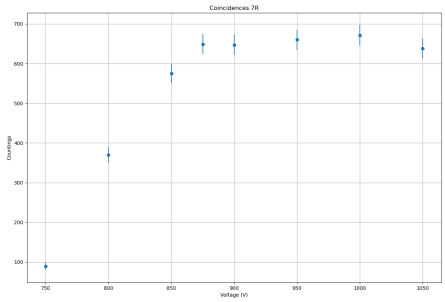

Figure A.27: Coincidence signals as a function of the applied voltage for PMT 7R.

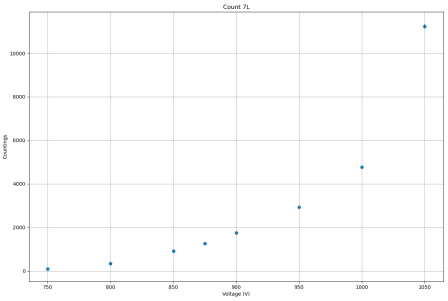

Figure A.28: Counting measure as a function of the applied voltage of PMT 7L.

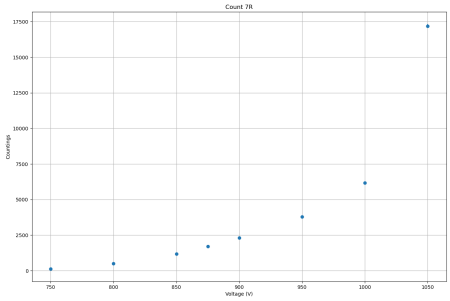

Figure A.29: Counting measure as a function of the applied voltage of PMT 7R.

Scintillator 8

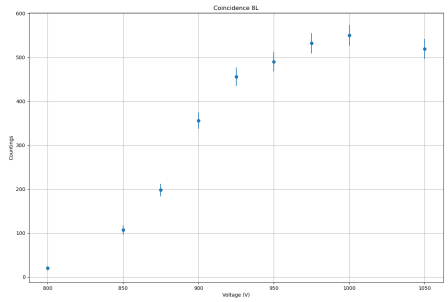

Figure A.30: Coincidence signals as a function of the applied voltage for PMT 8L.

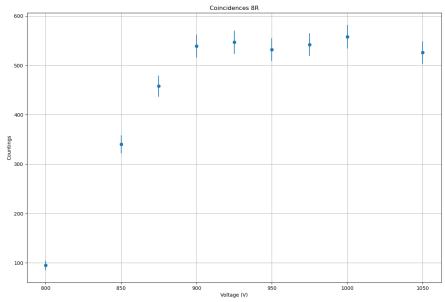

Figure A.31: Coincidence signals as a function of the applied voltage for PMT 8R.

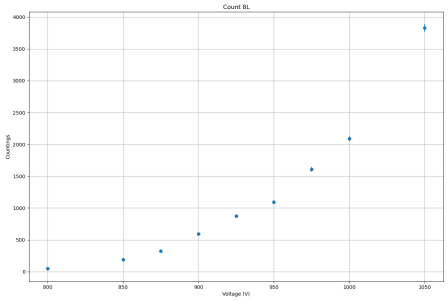

Figure A.32: Counting measure as a function of the applied voltage of PMT 8L.

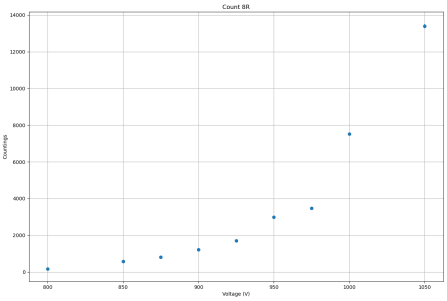

Figure A.33: Counting measure as a function of the applied voltage of PMT 8R.

Scintillator 9

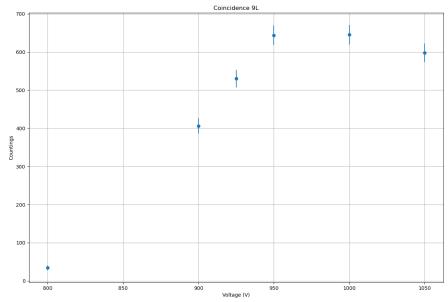

Figure A.34: Coincidence signals as a function of the applied voltage for PMT 9L.

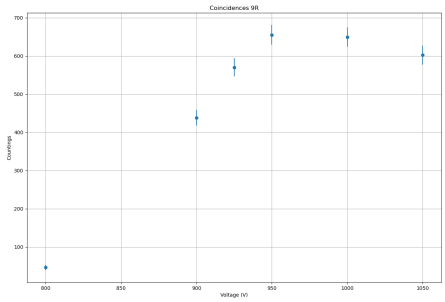

Figure A.35: Coincidence signals as a function of the applied voltage for PMT 9R.

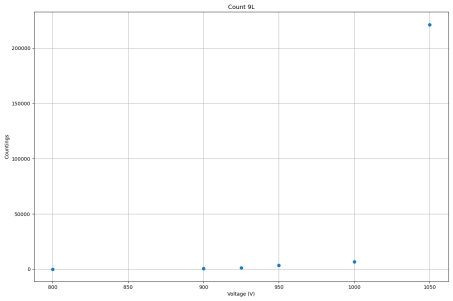

Figure A.36: Counting measure as a function of the applied voltage of PMT 9L.

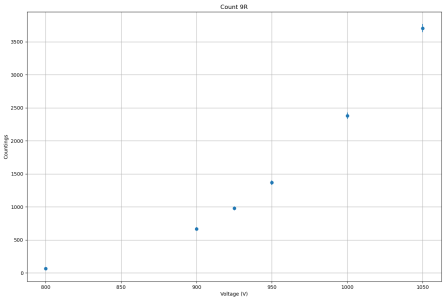

Figure A.37: Counting measure as a function of the applied voltage of PMT 9R.

Scintillator 10

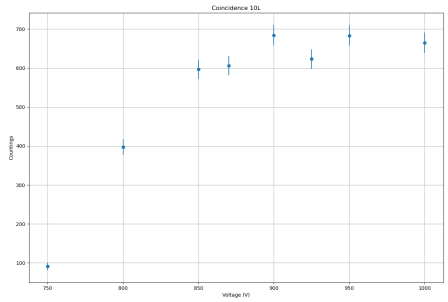

Figure A.38: Coincidence signals as a function of the applied voltage for PMT 10L.

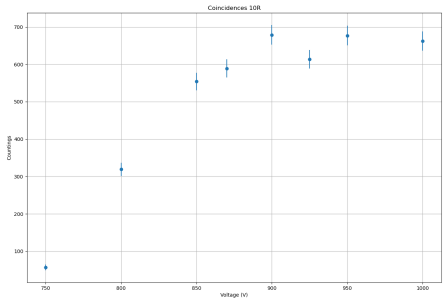

Figure A.39: Coincidence signals as a function of the applied voltage for PMT 10R.

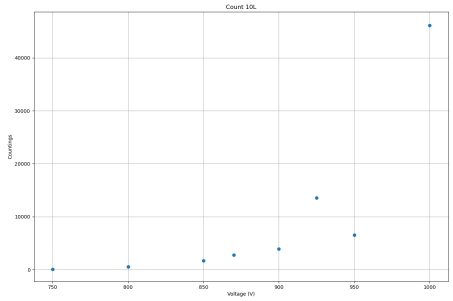

Figure A.40: Counting measure as a function of the applied voltage of PMT 10L.

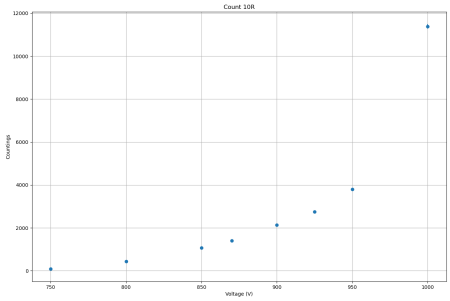

Figure A.41: Counting measure as a function of the applied voltage of PMT 10R.

Scintillator 11

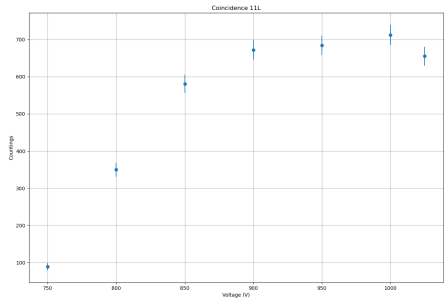

Figure A.42: Coincidence signals as a function of the applied voltage for PMT 11L.

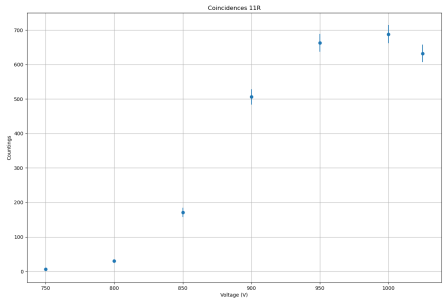

Figure A.43: Coincidence signals as a function of the applied voltage for PMT 11R.

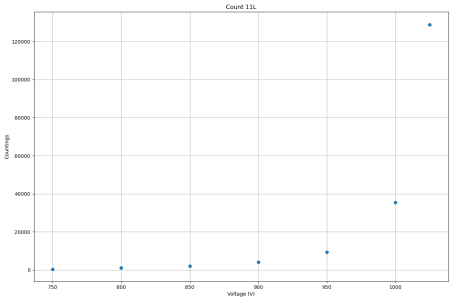

Figure A.44: Counting measure as a function of the applied voltage of PMT 11L.

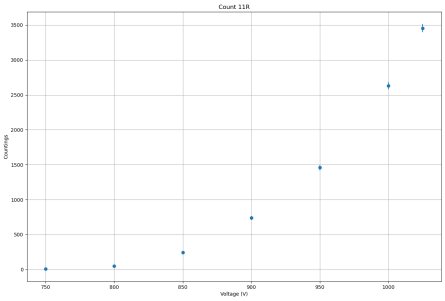

Figure A.45: Counting measure as a function of the applied voltage of PMT 11R.

Scintillator 12

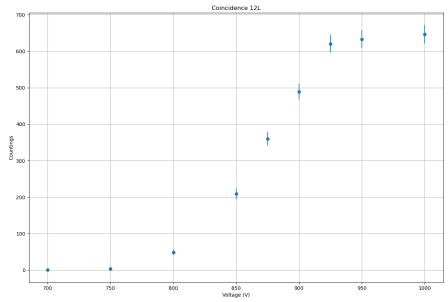

Figure A.46: Coincidence signals as a function of the applied voltage for PMT 12L.

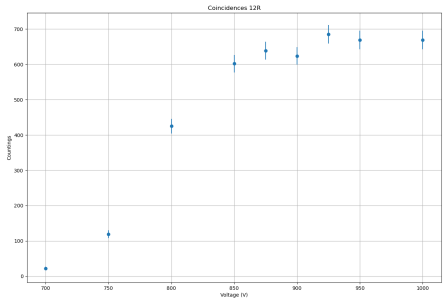

Figure A.47: Coincidence signals as a function of the applied voltage for PMT 12R.

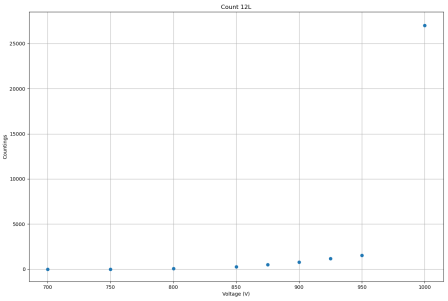

Figure A.48: Counting measure as a function of the applied voltage of PMT 12L.

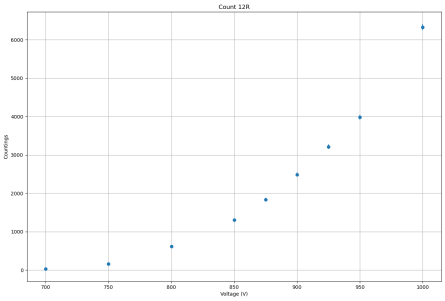

Figure A.49: Counting measure as a function of the applied voltage of PMT 12R.

Bibliography

[1] S. Chatrchyan et al. "The CMS Experiment at the CERN LHC". In: *JINST* 3 (2008), S08004. DOI: 10.1088/1748-0221/3/08/S08004.

[2] CMS Collaboration. "Performance of the CMS drift tube chambers with cosmic rays". In: *Journal of Instrumentation* 5.03 (2010), T03015–T03015. DOI: 10.1088/1748-0221/5/03/t03015. URL: https://doi.org/10.1088/1748-0221/5/03/t03015.

[3] J. G. Layter. *The CMS muon project: Technical Design Report*. Technical design report. CMS. Geneva: CERN, 1997. URL: http://cds.cern.ch/record/343814.

[4] Carlo Battilana. "Drift Tubes Trigger System of the CMS Experiment at LHC : Commissioning and Performances". Presented 2009. 2009. URL: https://cds.cern.ch/record/1328965.

[5] M Aguilar-Benìtez et al. "Construction and test of the final CMS Barrel Drift Tube Muon Chamber prototype". In: *Nuclear Instruments and Methods in Physics Research Section A: Accelerators, Spectrometers, Detectors and Associated Equipment* 480.2 (2002), pp. 658–669. ISSN: 0168-9002. DOI: https://doi.org/10.1016/S0168-9002(01)01227-X. URL: https://www.sciencedirect.com/science/article/pii/S016890020101227X.

[6] J Cela et al. "CMS Drift Tube Chambers Read-Out Electronics". In: *Proceedings of the Topical Workshop on Electronics for Particle Physics, TWEPP 2007* (2007).

[7] Á. Navarro-Tobar et al. "Phase 1 upgrade of the CMS drift tubes read-out system". In: *Journal of Instrumentation* 12.03 (2017), pp. C03070–C03070. DOI: 10.1088/1748-0221/12/03/c03070. URL: https://doi.org/10.1088/1748-0221/12/03/c03070.

[8] *Micro Telecommunications Computing Architecture Short Form Specification*. URL: https://www.picmg.org/wp-content/uploads/MicroTCA_Short_Form_Sept_2006.pdf.

[9] Andrea Triossi et al. "A New Data Concentrator for the CMS Muon Barrel Track Finder - Phase I Upgrade". In: *PoS* TIPP2014 (2015), p. 412. DOI: 10.22323/1.213.0412.

[10] CMS collaboration. "Performance of the CMS Level-1 trigger in proton-proton collisions at $\sqrt{s} = 13\,\text{TeV}$". In: *JINST* 15 (2020), P10017. 63 p. DOI: 10.1088/1748-0221/15/10/P10017. arXiv: 2006.10165. URL: https://cds.cern.ch/record/2721198.

[11] *DT Performance at the end of RUN-2*. URL: https://twiki.cern.ch/twiki/bin/view/CMSPublic/DtDPGResults18042019.

[12] A.M. Sirunyan et al. "Performance of the CMS muon detector and muon reconstruction with proton-proton collisions at $\sqrt{s} = 13\,\text{TeV}$". In: *Journal of Instrumentation* 13.06 (2018), P06015–P06015. DOI: 10.1088/1748-0221/13/06/p06015. URL: https://doi.org/10.1088/1748-0221/13/06/p06015.

[13] CMS Collaboration. *The Phase-2 Upgrade of the CMS Data Acquisition and High Level Trigger*. Tech. rep. Geneva: CERN, 2021. URL: https://cds.cern.ch/record/2759072.

[14] *The Phase-2 Upgrade of the CMS Muon Detectors*. Tech. rep. Geneva: CERN, 2017. URL: https://cds.cern.ch/record/2283189.

[15] Barbara Alvarez Gonzalez. *CMS Muon Drift Tubes HL-LHC Slice Test*. 2021. DOI: 10.48550/ARXIV.2110.15052. URL: https://arxiv.org/abs/2110.15052.

[16] Javier Sastre Alvaro. *The OBDT board: A prototype for the Phase 2 Drift Tubes on-detector electronics*. Tech. rep. Geneva: CERN, 2020. URL: https://cds.cern.ch/record/2797780.

[17] Andrea Triossi. *Electronics Developments for Phase-2 Upgrade of CMS Drift Tubes*. Tech. rep. Geneva: CERN, 2018. URL: https://cds.cern.ch/record/2645761.

[18] A Gabrielli et al. "The GBT-SCA, a radiation tolerant ASIC for detector control applications in SLHC experiments". In: (2009). DOI: 10.5170/CERN-2009-006.557. URL: https://cds.cern.ch/record/1235882.

[19] *lpGBT Documentation*. URL: https://cds.cern.ch/record/2809058/files/lpGBT_manual.pdf.

[20] Jan Troska et al. "The VTRx+, an Optical Link Module for Data Transmission at HL-LHC". In: Mar. 2018, p. 048. DOI: 10.22323/1.313.0048.

[21] *VC707 Evaluation Board for the Virtex-7 FPGA User Guide*. URL: https://www.xilinx.com/support/documents/boards_and_kits/vc707/ug885_VC707_Eval_Bd.pdf.

[22] *7 Series FPGA AMS Targeted Reference Design User Guide*. URL: https://docs.xilinx.com/v/u/2.0-English/ug960-7series-ams-trd-user-guide.

[23] C. Ghabrous Larrea et al. "IPbus: a flexible Ethernet-based control system for xTCA hardware". In: *Journal of Instrumentation* 10.02 (2015), pp. C02019–C02019. DOI: 10.1088/1748-0221/10/02/c02019. URL: https://doi.org/10.1088/1748-0221/10/02/c02019.

[24] *KCU105 Board User Guide*. URL: https://www.xilinx.com/support/documents/boards_and_kits/kcu105/ug917-kcu105-eval-bd.pdf.

[25] *UltraScale Architecture Configuration User Guide*. URL: https://www.xilinx.com/content/dam/xilinx/support/documents/user_guides/ug570-ultrascale-configuration.pdf.

[26] *FM-S14 Quad SFP/SFP+ transceiver FMC*. URL: https://www.fastertechnology.com/fileadmin/pdf-forms/S14_Product_Briefv2.pdf.

[27] *uHAL library. Part of the IPbus software repository*. URL: https://ipbus.web.cern.ch/sw/release/2.7/api/html/.

[28] *MiniDT Monitor Project*. URL: https://github.com/GiuliaPaggi/MiniDT_online_monitor.

[29] *Streamlit*. URL: https://streamlit.io/.

[30] *CMS Offline Software*. URL: https://github.com/cms-sw/cmssw.

[31] *DT NTuples Producer*. URL: https://github.com/battibass/DTNtuples.

[32] *DT Slice Test Offline Analysis Project*. URL: https://github.com/battibass/DTSliceTestOfflineAnalysis.

[33] G Abbiendi et al. "Offline calibration procedure of the CMS Drift Tube detectors". In: *Journal of Instrumentation* 4.05 (2009), P05002–P05002. DOI: 10.1088/1748-0221/4/05/p05002. URL: https://doi.org/10.1088/1748-0221/4/05/p05002.

[34] The CMS collaboration. "The performance of the CMS muon detector in proton-proton collisions at $\sqrt{s} = 7\,\text{TeV}$ at the LHC". In: *Journal of Instrumentation* 8.11 (2013). DOI: 10.1088/1748-0221/8/11/p11002.